Hybrid-Beamforming-Based Millimeter-Wave Cellular Network Optimization

Jia Liu, *Senior Member, IEEE,* and Elizabeth S. Bentley, *Member, IEEE*

***Abstract*—Massive MIMO and millimeter-wave communication (mmWave) have recently emerged as two key technologies for building 5G wireless networks and beyond. To reconcile the conflict between the large antenna arrays and the limited amount of radio-frequency (RF) chains in mmWave systems, the so-called hybrid beamforming becomes a promising solution and has received a great deal of attention in recent years. However, existing research on hybrid beamforming focused mostly on the physical layer or signal processing aspects. So far, there is a lack of theoretical understanding of how hybrid beamforming could affect mmWave *network optimization*. In this paper, we consider the impacts of hybrid beamforming on utility-optimality and queueing delay in mmWave cellular network optimization. Our contributions in this paper are three-fold: i) we develop a joint hybrid beamforming and congestion control algorithmic framework for mmWave network utility maximization; ii) we reveal a pseudoconvexity structure in the hybrid beamforming scheduling problem, which leads to simplified analog beamforming protocol design; and iii) we theoretically characterize the scalings of utility-optimality and delay with respect to channel state information (CSI) accuracy in digital beamforming.**

I. INTRODUCTION

In recent years, millimeter wave communication (mmWave) has emerged as a promising technology for building 5G wireless networks and beyond. The excitements of mmWave communications are primarily due to: i) the rich unlicensed spectrum resources in 60 GHz bands; ii) the ease of packing large antenna arrays into small form factors (a consequence of the short wavelengths); and iii) a much simplified interference management thanks to the highly directional "pencil-beam-like" mmWave signals. Moreover, recent field tests (see, e.g., [1], [2], etc.) have shown that the large directivity gains of mmWave transceivers can offset the high atmospheric attenuation in mmWave bands, dispelling the common concern that mmWave is not suitable for outdoor communications. The potential of mmWave networks has also stimulated many standardization activities (e.g., IEEE 802.15.3 wireless personal area networks, 802.11ad wireless local area networks, and fast-growing interests in mmWave cellular networks [3]).

However, the highly directional propagation of mmWave signals and the special mmWave hardware requirements also introduce several unique technical challenges for *networking systems*. One major problem in mmWave networking is its vulnerability to blockage, which is due to the weak diffraction ability of mmWave communications [3], [4]. Mitigating blockage in mobile cellular networks requires a frequent search for new unblocked directed spatial paths, which entails a large communication overhead and complicates the scheduling and congestion control algorithmic designs at higher layers. Another main technical challenge is *energy-efficient* beamforming architecture design, which lies at the heart of mmWave directional networking. Although large antenna arrays can be easily deployed in mmWave systems, the *high power consumption* of mixed mmWave signal components significantly limits the number of radio-frequency chains (RF chains), rendering full digital beamforming (requiring one RF chain per antenna) impractical [5]. Moreover, most of the digital beamforming schemes in traditional MIMO systems require full channel state information (CSI), which is difficult to acquire in mmWave systems due to the fast fading in mmWave spectrum and the low signal-to-noise ratio (SNR) before beamforming [6]. Because of the RF chain limitations in mmWave systems, analog beamforming approaches have been proposed (see, e.g., [7], [8]). The basic idea of analog beamforming is to control the phase shifters of antenna elements, so that the energy of the transmitted data stream is concentrated in a single direction to obtain a high directivity gain. Compared to digital beamforming, analog beamforming can be achieved by only one RF chain without requiring any CSI at the transmitter. However, analog beamforming can only transmit in a single beam direction and cannot leverage any spatial multiplexing capability of the large mmWave antenna array.

In light of the limitations of analog and digital beamformings, there is a growing consensus that the more suitable architecture for mmWave cellular networks is the *hybrid beamforming* architecture, which exploits the large mmWave antenna arrays and yet only requires a limited number of RF chains [6], [9]–[12]. Hybrid beamforming enjoys the best of both worlds: On one hand, it uses analog beamforming to offer spatial division and directivity gains to combat large mmWave channel attenuations. On the other hand, digital beamforming provides multiplexing gains for the lower dimensional *effective channels*, for which the CSI is relatively easier to acquire. It has been shown in [6], [13] that hybrid beamforming achieves a data rate performance comparable to full digital

---

Manuscript received May 22, 2019, revised September 10, 2019, and accepted October 4, 2019. This work is supported by NSF grants ECCS-1818791, CCF-1758736, CNS-1758757, CNS-1446582; ONR grant N00014-17-1-2417, and AFRL grant FA8750-18-1-0107. This paper was presented in part at IEEE/IFIP WiOpt, Paris, France, May 2017. Any opinions, findings and conclusions or recommendations expressed in this material are those of the author(s) and do not necessarily reflect the views of AFRL and ONR.

Jia Liu is with the Department of Computer Science, Iowa State University, Ames, IA, 50011 USA (e-mail: jialiu@iastate.edu).

Elizabeth S. Bentley is with the Air Force Research Laboratory, Information Directorate, Rome, NY, 13441 USA (e-mail: elizabeth.bentley.3@us.af.mil).

DISTRIBUTION STATEMENT A: Approved for Public Release; distribution unlimited 88ABW-2019-4902 on 09 October 2019. Other requests shall be referred to AFRL/RIT 525 Brooks Rd Rome, NY 13441.

Digital Object Identifier xx.xxxx/XXXX.xxxx.xxxxx.

beamforming with 8 to 16 times fewer RF chains.

So far, however, the existing works on mmWave hybrid beamforming are mostly concerned with problems at the physical layer or signal processing aspects. To date, there remains a lack of theoretical understanding on how hybrid beamforming could affect *mmWave networking performances* in terms of congestion control, scheduling, and resource optimization algorithms. In this paper, our goal is to fill this gap by conducting an in-depth study on the impacts of hybrid beamforming on throughput and delay performances in mmWave cellular network optimization.

Specifically, in this paper, we focus on the algorithmic design and the throughput-delay analysis for the celebrated queue-length-based congestion control and scheduling framework (QCS) (see, e.g., [14], [15], and [16] for a survey) in hybrid-beamforming-based mmWave cellular networks. Our main results and technical contributions are as follows:

- We develop an accurate analytical model that captures the essence of hybrid beamforming in mmWave cellular networks, while being tractable enough to enable network-level understanding and analysis. Based on this analytical model, we investigate the problem of joint hybrid beamforming and congestion control for network utility maximization. We show that the joint hybrid beamforming and congestion control optimization is non-convex by nature, which creates challenges for the algorithmic designs in the MaxWeight scheduling component in the QCS framework.
- By exploiting the special problem structure of the mmWave MaxWeight scheduling component, we show that the non-convex scheduling subproblem admits a pseudoconvex approximation under a wide range of hybrid beamforming parameters of practical interests. Moreover, our analysis reveals that, to solve the scheduling subproblem, one only needs to adjust the analog beamwidth at the base station (BS), while the analog beamwidth adjustment at the mobile station (MS) side is unnecessary. This insight greatly simplifies the analog beamforming training protocol design.
- We investigate the impact of CSI inaccuracy on network performance with hybrid beamforming, where we assume that the true CSI is quantized by Q bits. We reveal a pair of interesting phase transition phenomena in utility-optimality and delay in the following sense: There exists a critical value $Q^\sharp$ such that: i) if $0 < Q < Q^\sharp$, then the deviations of steady-state queue-length grows linearly and the congestion control rate is bounded by a constant; ii) If $Q \geq Q^\sharp$, the deviations of queue-lengths and congestion control rates have the same scaling laws as in the full CSI case.

Collectively, these results not only deepen our theoretical understanding of mmWave network optimization with hybrid beamforming, but also provide insights for low-complexity analog beam training and effective CSI quantization in practice. The remainder of this paper is organized as follows: In Section III, we introduce network models and the problem formulation. Section IV presents the mmWave congestion control and scheduling framework, as well as the algorithmic design for analog beam training. Section V studies the impacts of inaccurate CSI on digital beamforming. Section VI provides numerical results and Section VII concludes this paper.

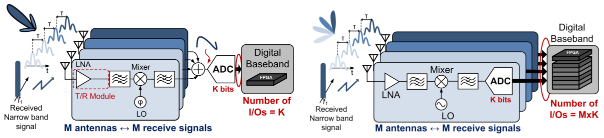

(a) (b)

Fig. 1. Traditional beamforming receiver architectures: (a) Analog beamforming using phase shifters along the signal path, and (b) and conventional digital beamformer using a separate ADC for each signal path.

II. Hybrid Beamforming: Background and Motivation

In this section, we provide a brief overview on the basics and the current state-of-knowledge related to MIMO beamforming techniques to further motivate the significance of hybrid beamformng for mmWave communications systems. Simply speaking, beamforming (also known as spatial filtering) is the ability for an antenna system to adaptively and electronically steer its beam along a desired direction while suppressing the reception of potential interferers from other directions. Depending on the "level of intelligence," beamforming can be classified into two major categories, namely *digital* and *anlalog* beamforming. Due to the symmetry (with reversed signal paths) between transmitter and receiver architecture, our discussions in this section are mostly focused on receiver design to avoid repetition. We note that most of the characteristics of receiver beamforming techniques apply similarly to the transmitter side.

1) Analog Beamforming: The basic idea of analog beamforming is to control the phase shifters of all antenna elements, so that the correlated transmitted and received signal energy is constructively combined at some desirable direction. A major advantage of analog beamforming at the RF front-end is the use of a single mixer to perform frequency translation. As such, the combined RF signal is down-converted to an intermediate frequency (IF) to be digitized by a *single* ADC for post-processing. This implies low energy consumption. However, due to the limited phase tuning, analog phase shifters can only sense a *single* spatial direction at a time [17]. That is, beams from multiple directions cannot be formed simultaneously, limiting the capability of the beamformer, particularly for MIMO applications. We note that this problem will be overcome by the hybrid beamforming architecture in Section III. Also, phase shifters suffer from high losses and bandwidth limitations. This is even more exacerbated for large antenna arrays as they require a large number of phase shifters. As a result, traditional analog beamformers suffer from large size, weight, and complexity of the array, and not to mention power consumption.

For wideband operations in mmWave, bandwidth limitation can be overcome by local oscillator (LO) phase-shifting, where a tunable oscillator is used to sweep the bandwidth [18]. However, the demand for fine phase resolution, necessary in reliable scanning, implies extreme hardware complexity. In addition, traditional analog beamformers have other drawbacks. Among them are: i) beamforming performance suffers from quantized levels of phase increments, ii) retraining of the phase shifting network implies processing overhead and sacrificing data throughput, iii) have significant hardware complexity that impacts size, power, and cost, and iv) do not accommodate spatial multiplexing unless a hybrid architecture is used.

2) Digital Beamforming: The aforementioned pitfalls of analog beamforming motivate the design of digital beamforming. For wideband operations, digital beamforming approaches offer more flexibility [19], [20] since beamforming and related adaptive algorithms are carried out at the back-end of the transceiver using FPGAs or other digital processing units. In digital beamforming, the RF signal is processed and digitized prior to amplitude scaling and phase shifting, as depicted in Fig. 1(b). To perform beamforming, the digitized baseband signal y_n is multiplied by a complex weight w_n for the n-th signal path. Therefore, the output is $y_{\text{out}} = \sum_n y_n w_n$, where the complex weight can be written as $w_n = a_n e^{\phi_n}$. Digital adaptive beamformers can achieve more accurate main beams, null steering, side lobes levels control, simultaneous multi-directional beams, and spatial multiplexing. However, existing digital beamformers at baseband have extensive hardware requirements as they employ separate ADCs for each signal path, as shown in Fig. 1(b). The large number of high-cost and power-hungry ADCs results in excessive power consumption in the back-end circuitry, making such approaches limited to small arrays. Further, most digital beamforming techniques for traditional MIMO require the full knowledge of channel state information (CSI), which is difficult to acquire for the large antenna array deployed in mmWave platforms.

To address the limitations of analog and digital beamforming, in the next section, we will introduce the analytic model of the cellular hybrid beamforming architecture, which achieves the best of both worlds of analog and digital beamforming.

III. NETWORK MODEL AND PROBLEM FORMULATION

Notation: We use boldface to denote matrices/vectors. $\mathbf{A}^\dagger$ denotes the conjugate transpose of $\mathbf{A}$. We use $\|\cdot\|$ and $\|\cdot\|_1$ to denote ℓ_2- and ℓ_1-norms, respectively. We let $\mathbf{I}$ denote the identity matrix, whose dimension is conformal to the context. We let $\mathbb{R}$ and $\mathbb{C}$ denote real and complex spaces, respectively.

1) Hybrid-Beamforming-Based mmWave Downlink: As shown in Fig. 2, we consider a mmWave cellular downlink system with N users. The BS and each user have M_{BS} and M_{MS} antennas, respectively. The mmWave downlink adopts a hybrid beamforming architecture with M_{RF}^{B} and M_{RF}^{M} RF chains at the BS and each user's MS, respectively (see Fig. 3). The system operates in a time-slotted mode. The time-slots are indexed by $t \in \{0, 1, 2, \ldots\}$. As shown in Fig. 4, each time-slot is of period T and contains two phases. The first phase is further divided into N mini-slots corresponding to the N users. Each mini-slot contains two parts τ_n^A and τ_n^D. In τ_n^A, both the BS and a user n perform analog beam search to refresh their beam directions to mitigate link breakage caused by user n's movements [3], [4]. In τ_n^D, the BS estimates the CSI of user n for digital beamforming. In the data transmission phase, based on the analog beam and digital CSI training results, the BS picks one of the N users and steers analog beams to this user. Likewise, the scheduled user also steers analog beams toward the BS. Further, by leveraging the learned CSI to perform spatial multiplexing, the BS and a scheduled user communicate via K data streams. For mmWave systems in practice, we usually have: i) $K \leq M_{\text{RF}}^{\text{B}} \leq M_{\text{BS}}$; ii) $K \leq M_{\text{RF}}^{\text{M}} \leq M_{\text{MS}}$; iii) $M_{\text{RF}}^{\text{M}} \leq M_{\text{RF}}^{\text{B}}$; and iv) $M_{\text{MS}} \leq M_{\text{BS}}$.

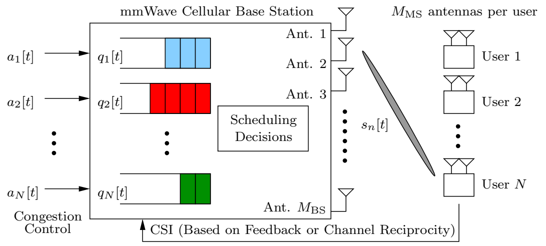

Fig. 2. A mmWave cellular downlink with a M_{BS}-antenna base station and N M_{MS}-antenna users.

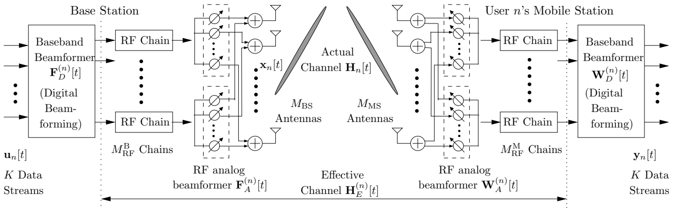

Fig. 3. Block diagram of a mmWave cellular network with hybrid beamforming.

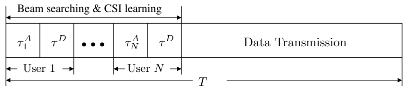

Fig. 4. Frame structure of a time-slot in mmWave cellular networks with hybrid beamforming.

a) Analog beamforming process: In time-slot t, the analog beamformers on the BS and user sides are determined by a beam training process, during which the BS and user n search over all possible direction combinations within their corresponding sectors[1], as shown in Fig. 5 (this exhaustive beam training process has been adopted in IEEE 802.11ad and IEEE 802.15.3c standards). Let T_p denote the time required for transmitting and receiving a pilot symbol. Let ψ_n^{B} and ψ_n^{M} denote the sector-level beamwidth at the BS and user n, respectively. Also, let $\theta_B[t]$ and $\theta_n[t]$ denote the beam-level beamwidth at the BS and user n's MS, respectively. Then, the beam search time τ_n^A can be computed as: $\tau_n^A = \frac{\psi_n^{\text{B}}}{\theta_B[t]} \frac{\psi_n^{\text{M}}}{\theta_n[t]} T_p$.

In this paper, we adopt a widely used sectored antenna pattern model (see, e.g., [21]–[23]): We assume that the gains are a constant for all angles within the main lobe and equal to a smaller constant in the side lobes. As shown in Fig. 5, we let ω_n^{B} and ω_n^{M} represent the angles deviating from the strongest path between the BS and user n, respectively (the strongest path needs not be line-of-sight and Fig. 5 is only for illustrative purposes). Let $g_n^{\text{B}}(\omega_n^{\text{B}}, \theta_B[t])$ and $g_n^{\text{M}}(\omega_n^{\text{M}}, \theta_n[t])$ denote the transmission and reception gains at the BS and user n. In this paper, we adopt the following widely used antenna radiation

---

[1] In this paper, we assume that both the BS and user know the sectors of each other's location in each time-slot. This is a reasonable assumption because the sector information can be inferred with high accuracy from the beam direction in the previous time-slot and the mobility/trajectory information of the user.

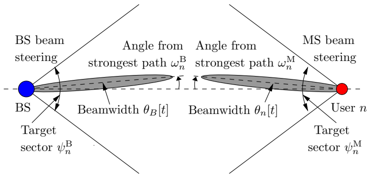

Fig. 5. The analog beamforming training procedure.

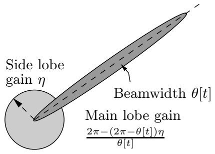

Fig. 6. The simplified antenna radiation pattern.

pattern model [21]–[23] (see Fig. 6):

$$g_n^{\mathrm{B}}(\omega_n^{\mathrm{B}}, \theta_B[t]) = \begin{cases} \frac{2\pi-(2\pi-\theta_B[t])\eta}{\theta_B[t]}, & \text{if } |\omega_n^{\mathrm{B}}| \leq \frac{\theta_B[t]}{2}, \\ \eta, & \text{otherwise,} \end{cases} \quad (1)$$

$$g_n^{\mathrm{M}}(\omega_n^{\mathrm{M}}, \theta_n[t]) = \begin{cases} \frac{2\pi-(2\pi-\theta_M[t])\eta}{\theta_n[t]}, & \text{if } |\omega_n^{\mathrm{M}}| \leq \frac{\theta_n[t]}{2}, \\ \eta, & \text{otherwise.} \end{cases} \quad (2)$$

where $\eta \in [0, 1)$ is the side lobe gain. In practice, $\eta \ll 1$ for narrow beams (i.e., $\theta_B[t]$ and $\theta_n[t]$ are small). This model captures the essential features of antenna patterns (e.g., directive gains, front-to-back ratio, half-power beamwidth, etc. [23]). Once the optimal directions for transmission and reception have been determined, the communication link can be established, and data transmission phase starts. The beam training is finished when the BS and the user's beams are aligned with the strongest path, i.e., the conditions $|\omega_n^{\mathrm{B}}| \leq \frac{\theta_B[t]}{2}$ in (1) and $|\omega_n^{\mathrm{M}}| \leq \frac{\theta_n[t]}{2}$ in (2) are satisfied.

b) Digital beamforming process: Once the analog beam search is completed, the analog beamformers are known. Therefore, we can estimate the CSI of the effective channel $\mathbf{H}_E^{(n)}[t]$, which is assumed to take $\tau^D = \beta T_p$ amount of time (cf. Fig. 4), where $\beta > 0$ is some constant. With the learned CSI, the BS and user n jointly choose baseband beamformers based on some digital beamforming strategies, such as singular value decomposition (SVD), zero-forcing (ZF), etc. One particularly interesting case arises when $M_{\mathrm{RF}}^{\mathrm{B}} \gg M_{\mathrm{RF}}^{\mathrm{M}}$. In this case, the row vectors in the effective channel $\mathbf{H}_E^{(n)}[t]$ are asymptotically orthogonal to each other as $M_{\mathrm{RF}}^{\mathrm{B}}$ gets large. Thanks to this nice property, one can use the so-called conjugate beamforming, which has been shown to be asymptotically capacity-achieving in the high SNR regime [24]. We will further discuss conjugate beamforming in Section V.

Regardless the choice of digital beamforming schemes, the digital beamforming process converts $\mathbf{H}_E^{(n)}[t]$ into $K \leq \min\{M_{\mathrm{RF}}^{\mathrm{B}}, M_{\mathrm{RF}}^{\mathrm{M}}\}$ spatial channels (depending on the rank of $\mathbf{H}_E^{(n)}[t]$). We let $g_n^{(k)}[t]$ denote the effective gain of the k-th spatial channel. Based on the models of hybrid analog/digital beamforming, we have that the hybrid beamforming achievable rate of user n can be computed as:[2]

$$r_n(\theta_B[t], \theta_n[t]) = \left(1 - \frac{\tau^A + N\tau^D}{T}\right) \sum_{k=1}^{K} \log_2 \Bigg(1 + \frac{P_{\max}}{KN_0} g_n^{\mathrm{B}}(\omega_n^{\mathrm{B}}, \theta_B[t]) g_n^{\mathrm{M}}(\omega_n^{\mathrm{M}}, \theta_M[t]) g_n^{(k)}[t]\Bigg), \quad (3)$$

where $\tau^A \triangleq \sum_{n=1}^{N} \tau_n^A$ and $P_{\max}$ denotes the maximum transmission power at the BS. Then, for a given channel state in time-slot t, we let $\mathcal{C}_n[t]$ denote the instantaneous achievable rate region under a chosen digital beamforming scheme:

$$\mathcal{C}_n[t] \triangleq \left\{ r_n(\theta_B[t], \theta_n[t]) \;\middle|\; \begin{array}{l} \theta_B[t] \in (0, \psi_n^{\mathrm{B}}], \\ \theta_M[t] \in (0, \psi_n^{\mathrm{M}}] \end{array} \right\}. \quad (4)$$

It can be seen from (3) that the beamwidths $\theta_B[t]$ and $\theta_n[t]$ need to be chosen judiciously: On one hand, from (1) and (2), $g_n^{\mathrm{B}}(\omega_n^{\mathrm{B}}, \theta_B[t])$ and $g_n^{\mathrm{M}}(\omega_n^{\mathrm{M}}, \theta_n[t])$ increase as $\theta_B[t]$ and $\theta_n[t]$ decrease, leading to a higher SNR and hence a higher data rate. However, the smaller the beamwidths $\theta_B[t]$ and $\theta_n[t]$, the shorter the transmission phase, i.e., there exists a *trade-off* between data rate and transmission time.

2) Queueing Model: As shown in Fig. 2, the BS maintains a separate queue for each user. Let $a_n[t]$ denote the number of packets injected into queue n in time-slot t. The arrival processes $\{a_n[t]\}$, $\forall n$, are controlled by a congestion controller. We assume that there exists a finite constant $A^{\max}$ such that $a_n[t] \leq A^{\max}$, $\forall n, t$. Let $\mathbf{s}[t] \triangleq [s_1[t], \ldots, s_N[t]]^\top$ denote the scheduled service rate vector in time-slot t (the scheduling algorithm that determines $\mathbf{s}[t]$ will be presented in Section IV). Then, the queue-length of user n evolves as: $q_n[t+1] = \big(q_n[t] - s_n[t] + a_n[t]\big)^+$, $\forall n$, where $(\cdot)^+ \triangleq \max(0, \cdot)$. Let $\mathbf{q}[t] = [q_1[t]], \ldots, q_N[t]]^\top$. In this paper, we adopt the following notion of queue-stability (same as in [14], [15]): We say that a network is *stable* if the steady-state total queue-length is finite, i.e., $\limsup_{t\to\infty} \mathbb{E}\{\|\mathbf{q}[t]\|_1\} < \infty$.

3) Problem Formulation: Let $\bar{a}_n \triangleq \lim_{T\to\infty} \frac{1}{T} \sum_{t=0}^{T-1} a_n[t]$ denote the average controlled arrival rate of user n. We associate each user n with a utility function $U_n(\bar{a}_n)$, which is assumed to be strongly concave, increasing, and twice continuously differentiable. $U_n(\bar{a}_n)$ represents the utility gained by user n when data is injected at rate $\bar{a}_n$. Then, the joint congestion control and scheduling (JCS) optimization problem for network utility maximization can be written as:

$$\begin{array}{lll} \textbf{JCS:} & \text{Maximize} & \sum_{n=1}^{N} U_n(\bar{a}_n) \\ & \text{subject to} & \text{Queue-length stability constraints,} \\ & & s_n[t] \in \mathcal{C}_n[t],\ a_n[t] \in [0, A^{\max}]\ \forall n, t. \end{array}$$

In Section IV, we will first consider the algorithmic design for solving Problem JCS under perfect CSI. Then, in Section V, we will conduct an in-depth investigation on the impacts of CSI inaccuracy on throughput and delay.

IV. ALGORITHMIC DESIGN UNDER PERFECT CSI

Because of the utility maximization formulation, Problem JCS can potentially be solved by the well-known queue-length-based congestion control and scheduling (QCS) framework (see, e.g., [14]–[16]) in the following sense: The congestion control rate $\bar{\mathbf{a}}$ achieves an optimality gap $O(\epsilon)$ at the price of an $O(1/\epsilon)$ queue-length, where $\epsilon > 0$ controls the utility-optimality gap. Hence, the utility-optimality gap can be made arbitrarily small by decreasing ϵ. We note that the queue-length-based congestion control mechanism is different and not to be confused with conventional TCP congestion control mechanism. Based on this insight, let us consider the following QCS algorithm specialized for hybrid beamforming in mmWave networks:

---

[2] In this paper, equal power allocation is used for lower rate evaluation complexity in the effective MIMO channel. This is because it has been shown that the rate loss of equal power allocation is negligible under moderate and high SNR regimes. Also, equal power allocation is asymptotically capacity-achieving in high SNR regime [25].

A. The QCS Algorithm Specialized for Hybrid Beamforming

Algorithm 1: Queue-Length-Based Joint Congestion Control and Scheduling for mmWave-Based Cellular Networks.

Initialization: Choose parameters $\epsilon > 0$. Set $t = 0$.
Main Loop:

1. *MaxWeight Scheduler:* In time $t \geq 1$, given queue-lengths $\mathbf{q}[t]$ and CSI $\mathbf{H}[t]$, the scheduler chooses a service rate vector $\mathbf{s}[t]$ from $\mathcal{C}_n[t]$ by hybrid beamforming such that:
$$\mathbf{s}[t] = \underset{r_n \in \mathcal{C}_n[t], \forall n}{\arg\max} \left\{ \sum_{n=1}^{N} q_n[t] r_n \right\}, \tag{5}$$
where $\mathcal{C}_n[t]$ is defined in (4).
2. *Congestion Controller:* Given queue-lengths $\mathbf{q}[t]$, the congestion controller chooses data injection rates $a_n[t]$, $\forall n$, which are integer-valued random variables satisfying:
$$\mathbb{E}\{a_n[t] | q_n[t]\} = \min \left\{ U_n^{'-1}\left(\epsilon q_n[t]\right), A^{\max} \right\}, \tag{6}$$
$$\mathbb{E}\{a_n^2[t] | q_n[t]\} \leq A_2^{\max} < \infty, \quad \forall q_n[t], \tag{7}$$
where $U_n^{'-1}(\cdot)$ represents the inverse function of first-order derivative of $U_n(\cdot)$. In (6) and (7), $A^{\max}$ and $A_2^{\max}$ are some predefined sufficiently large positive constants.
3. *Queue-Length Updates:* Update the queue-lengths as $q_n[t+1] = (q_n[t] - s_n[t] + a_n[t])^+$, $\forall n$. Let $t = t+1$. Go to Step 1 and repeat the process.

It can be shown that Algorithm 1 is utility-optimal if the optimization subproblems in (5) and (6) can be solved to optimality in each iteration. However, the QCS framework has a major limitation in that the MaxWeight scheduling problem is difficult to solve in general and could be NP-Hard in many wireless networks [16]. Surprisingly, in what follows, we will show that the physical layer properties of hybrid beamforming actually imply several special mathematical structures that leads to efficient solution for the MaxWeight subproblem.

B. The MaxWeight Scheduling Subproblem

To solve the MaxWeight scheduling subproblem, we start by examining the properties of the set of instantaneous hybrid beamforming achievable rates $\{r_n \in \mathcal{C}_n[t], \forall n\}$. First, we note that the BS forms only one beam to one of the N users in each time-slot, say user n. This implies that $r_{n'} = 0$, $\forall n' \neq n$. Hence, the MaxWeight problem in (5) can be simplified as:

$$\max_{r_n \in \mathcal{C}_n[t], \forall n} \left\{ \sum_{n=1}^{N} q_n[t] r_n \right\} = \max_{n \in \{1,\dots,N\}} \left\{ q_n[t] r_n \middle| r_n \in \mathcal{C}_n[t] \right\}$$
$$\overset{(a)}{=} \max_{n \in \{1,\dots,N\}} \left\{ q_n[t] \left[\max_{\theta_B[t], \theta_n[t]} \left\{ r_n(\theta_B[t], \theta_n[t]) \right\} \right] \right\}, \tag{8}$$

where (a) follows from the fact that $r_n(\theta_B[t], \theta_n[t])$ does not depend on $q_n[t]$. As a result, solving the MaxWeight scheduling problem in (5) boils down to first solving the inner rate maximization problem in (8) for each user, and then choosing the user who has the largest rate-queue-length product. Toward this end, we explicitly write down the inner maximization problem in (8) for each user n as follows:

$$\begin{aligned} \text{Maximize} \quad & \left(1 - \frac{\tau^A + \tau^D}{T}\right) \sum_{k=1}^{K} \log_2 \bigg(1 + \frac{P_{\max}}{K N_0} \\ & \qquad g_n^{\mathrm{B}}(\omega_n^{\mathrm{B}}, \theta_B[t]) g_n^{\mathrm{M}}(\omega_n^{\mathrm{M}}, \theta_n[t]) g_n^{(k)}[t] \bigg) \\ \text{subject to} \quad & \theta_B[t] \in (0, \psi_n^{\mathrm{B}}], \ \theta_n[t] \in (0, \psi_n^{\mathrm{M}}]. \end{aligned} \tag{9}$$

Unfortunately, due to the multiplication between the time fraction and the rate in the objective function, Problem (9) falls into the class of *generalized polynomial programming* problems, which is non-convex and NP-Hard [26]. In this paper, we consider a slightly modified and yet practically relevant homogenous setting: All users in each time-slot have the same beamwdith $\theta_n[t] = \theta_{\mathrm{M}}[t]$, $\forall n$, where $\theta_{\mathrm{M}}[t]$ denotes the common beamwidth of all users in time t, which can be facilitated through BS coordination. Under the homogenous setting, Problem (9) *remains* a non-convex polynomial program. However, it turns out that if the side lobe gain η is small, Problem (9) can be approximated by a univariate pseudoconvex problem as stated below:

Lemma 1 (Univariate approximation). *If the side lobe gain satisfies $\eta \ll \frac{1}{3}$, then Problem (9) can be approximated by the following univariate optimization problem:*

$$\begin{aligned} \text{Maximize} \quad & \left(b_0 - \frac{b_1}{\tilde{\theta}[t]}\right) \sum_{k=1}^{K} \log_2 \left(1 + \frac{4\pi^2 c_n^{(k)}}{\tilde{\theta}[t]}\right) \\ \text{subject to} \quad & \tilde{\theta}[t] \in \left[\frac{b_1}{b_0}, \ \psi_n^{\mathrm{B}} \psi_n^{\mathrm{M}}\right], \end{aligned} \tag{10}$$

where $b_0 \triangleq 1 - (N\beta T_p / T)$, $b_1 \triangleq \frac{T_p}{T} \sum_{n=1}^{N} \psi_n^{\mathrm{B}} \psi_n^{\mathrm{M}}$, and $c_n^{(k)} \triangleq (P_{\max}/K N_0) g_n^{(k)}[t]$ are constants.

Lemma 1 can be proved by substituting the antenna radiation pattern model in (1) and (2) into the objective function of Problem (9) and then exploiting the condition $\eta \ll \frac{1}{3}$ to simplify. We relegate the proof details to Appendix A. With Lemma 1, we now state the first main result of this paper:

Theorem 1 (Pseudoconvexity[3] of the approximation). *Problem (10) is a pseudoconvex optimization problem. Moreover, if $T_p \ll T$, then Problem (10) has one unique maximum achieved in the interior of $[b_1/b_0, \psi_n^{\mathrm{B}} \psi_n^{\mathrm{M}}]$.*

Since Problem (10) is a maximization problem with one simple box constraint, showing its pseudoconvexity is equivalent to showing the pseudoconcavity of the objective function. We refer readers to Appendix B for proof details.

Remark 1. Three remarks of Lemma 1 and Theorem 1 are in order: i) In practice, the conditions $T_p \ll T$ and $\eta \ll \frac{1}{3}$ can usually be satisfied because a pilot symbol is much shorter compared to a time-slot and the mmWave beams are sharp; ii) The pseudoconvex (which further implies strictly quasiconvex) and univariate properties suggest that Problem (10) can be solved by simple one-dimensional line search methods [26, Theorem 8.1.1] (e.g., the bisection or the golden section

---

[3] In convex analysis, a function $f: S \in \mathbb{R}^N \to \mathbb{R}$ is said to be pseudoconvex if for each $\mathbf{x}_1, \mathbf{x}_2 \in S$, $\nabla f(\mathbf{x}_1)^\top (\mathbf{x}_2 - \mathbf{x}_1) \geq 0$ implies $f(\mathbf{x}_2) \geq f(\mathbf{x}_1)$ or equivalently $\nabla f(\mathbf{x}_2)^\top (\mathbf{x}_2 - \mathbf{x}_1) \geq 0$. The function f is said to be pseudoconcave if $-f$ is pseudoconvex.

methods); iii) It can be seen from the proof of Lemma 1 that we have defined $\tilde{\theta}[t] \triangleq \theta_B[t]\theta_{\mathrm{M}}[t]$. Note that the optimal objective value of Problem (10) is only a function of $\tilde{\theta}^*[t]$ and does not depend on the specific values of $\theta_B[t]$ and $\theta_{\mathrm{M}}[t]$, as long as their product is equal to $\tilde{\theta}^*[t]$. This implies that we can simply set $\theta_{\mathrm{M}}[t]$ to some appropriate fixed value and only adjust $\theta_{\mathrm{B}}[t]$ at the BS side. In other words, there is no need to jointly adjust $\theta_{\mathrm{B}}[t]$ and $\theta_{\mathrm{M}}[t]$. This insight greatly simplifies the protocol designs in the analog beamforming phase. □

Collectively, the results in this section provide an algorithmic solution to Problem JCS assuming that the CSI learned in τ^D (hence the digital beamforming gains $g_n^{(k)}[t]$) is accurate. However, it remains unclear how the network utility and delay performance of Algorithm 1 will be affected if the CSI is inaccurate. This problem will be addressed in the next section.

V. THE IMPACTS OF INACCURATE CSI ON THE QCS ALGORITHM WITH HYBRID BEAMFORMING

Generally speaking, in traditional multi-antenna networks, CSI is measured at each MS based on pilot symbol training and then fed back to the BS. However, due to the short coherence time of mmWave channels (around an order of magnitude lower than that of microwave bands since Doppler shifts scale linearly with frequencies [3]), this traditional CSI feedback approach is not suitable for mmWave-based cellular networks. Another CSI acquisition method is to have the system run in time-division duplexing (TDD) mode. Based on the channel reciprocity, the uplink CSI measured at the BS will be used for downlink transmissions. However, the limited transmit power at the MSs and the lack of beamforming gains for the uplink pilot symbols limit the accuracy of TDD-based CSI estimation. Further, the short coherence time of mmWave bands implies that the channel reciprocity assumption is only valid for low-mobility scenarios. Given these CSI estimation challenges in mmWave cellular systems, it is likely that the CSI learned during the τ^D period (cf. Fig. 4) is inaccurate.

In studying the impacts of CSI inaccuracy, we are interested in the case where the number of RF chains at the BS is much greater than that at the MSs (e.g., 10 times larger). This setting is particularly interesting because it is the relevant case for mmWave cellular networks in practice: First, as mentioned in Section I, large antenna arrays can be easily deployed at the BS due to the short wavelengths of mmWave bands. Also, because of the physical size and power constraints, the MSs usually accommodate much fewer RF chains compared to that at the BS side. Moreover, as noted in many studies [24], CSI acquisition is one of the most fundamental limiting factors in the system designs of large-scale antenna cellular systems. In what follows, we start with the digital beamforming for effective mmWave channels with a large number of RF chains at the BS and its operations under a limited CSI model.

1) Digital Beamforming for Effective Channels: As mentioned in Section III, if $M_{\mathrm{RF}}^{\mathrm{B}} \gg M_{\mathrm{RF}}^{\mathrm{M}}$, due to the near orthogonality between the rows in the effective channel in this case, the simple conjugate digital beamforming technique from the Massive MIMO literature and related queueing network techniques [27], [28] can be adopted[4]. Recall that the received signal of user n can be written as: $\mathbf{y}[t] = \mathbf{W}_D^{(n)\dagger}[t]\mathbf{H}_E^{(n)}[t]\mathbf{F}_D^{(n)}[t]\mathbf{u}_n[t] + \tilde{\mathbf{n}}[t]$, where $\mathbf{H}_E^{(n)}[t] \in \mathbb{C}^{M_{\mathrm{RF}}^{\mathrm{M}} \times M_{\mathrm{RF}}^{\mathrm{B}}}$ is the effective channel by taking into account the effects of analog beamforming; and $\mathbf{F}_D^{(n)}[t]$ and $\mathbf{W}_D^{(n)\dagger}[t]$ are the transmit and receive digital beamformers, respectively. Under conjugate beamforming, we have $\mathbf{W}_D^{(n)\dagger}[t] = \mathbf{I}$ and $\mathbf{F}_D^{(n)}[t] = \mathbf{H}_E^{(n)}[t]^\dagger$, i.e., the conjugate transpose of $\mathbf{H}_E^{(n)}[t]$. Also, we assume that the effective channel $\mathbf{H}_E^{(n)}[t]$ is of full row rank so that we can let $K = M_{\mathrm{RF}}^{\mathrm{M}}$ (i.e., all receiver RF chains are utilized). Then, the achievable rate under digital conjugate beamforming can be approximately computed as:

$$r_n[t] \approx \left(1 - \frac{\tau^A + \tau^D}{T}\right) \sum_{k=1}^{K} \log_2\left(1 + \frac{P_{\max}}{K N_0} \|\mathbf{h}_{E,k}^{(n)}[t]\|^2\right), \quad (11)$$

where $\mathbf{h}_{E,k}^{(n)}[t]$ denotes the k-th row of $\mathbf{H}_E^{(n)}[t]$. In (11), the approximation holds because the rows of $\mathbf{H}_E^{(n)}[t]$ are nearly orthogonal as $M_{\mathrm{RF}}^{\mathrm{B}}$ gets large. Note that in $\mathbf{h}_{E,k}^{(n)}[t]$ in (11), we have absorbed the array gains $g_n^{\mathrm{B}}(\omega_n^{\mathrm{B}}, \theta_B[t])$ and $g_n^{\mathrm{M}}(\omega_n^{\mathrm{M}}, \theta_n[t])$ (cf. Eq. (3)) achieved by analog beamforming.

2) CSI Inaccuracy Modeling: Given the inevitable CSI errors and to alleviate the CSI estimation burden for digital beamforming, we adopt the limited CSI model in the literature (see, e.g., [25] and references therein). Such limited CSI can be obtained by Q bits of feedback from each user. Alternatively, based on the channel reciprocity, the BS could use Q bits to rapidly quantize the uplink CSI (see Fig. 2). In either case, the value of Q depends on the CSI learning time τ^D and efficiency of the specific CSI learning algorithm. The Q-bit limited CSI for each RF chain k can be determined by a vector quantization codebook $\mathcal{B}_k \triangleq \{\mathbf{c}_k^1, \ldots, \mathbf{c}_k^{2^Q}\}$, where $\mathbf{c}_k^i \in \mathbb{C}^{M_{\mathrm{RF}}^{\mathrm{B}}}$, $i = 1, \ldots, 2^Q$, represents a codeword. Given an effective channel $\mathbf{H}_E^{(n)}[t]$, the codeword for its k-th row vector $\mathbf{h}_{E,k}^{(n)}[t]$ is chosen by picking the one that is closest to $\mathbf{h}_{E,k}^{(n)}[t]$ in the following sense [25]: $i_k^*[t] = \arg\min_{j \in \{1,\ldots,2^Q\}} \sin^2(\angle(\mathbf{h}_{E,k}^{(n)}[t], \mathbf{c}_n^j))$, where $i_k^*[t]$ denotes the index of the chosen codeword in time-slot t. Let $\widehat{\mathbf{H}}_E^{(n)}[t] \in \mathbb{C}^{M_{\mathrm{RF}}^{\mathrm{M}} \times M_{\mathrm{RF}}^{\mathrm{B}}}$ denote the estimated channel matrix by collecting all codewords $i_k^*[t]$, $\forall k$. Then, based on $\widehat{\mathbf{H}}_E^{(n)}[t]$, the BS performs conjugate beamforming to construct K spatial channels. However, due to the errors in $\widehat{\mathbf{H}}_E^{(n)}[t]$, inter-channel interference is not negligible under conjugate beamforming, and the amount of interference depends on the codebook size 2^Q and the choice of the quantization scheme.

Let $\widehat{r}_n^Q[t]$ denote the actual conjugate beamforming achievable rate under the true CSI $\mathbf{H}_E^{(n)}[t]$ while the system is treating the Q-bit limited CSI $\widehat{\mathbf{H}}_E^{(n)}[t]$ as if it is accurate. Also, let $\widehat{\mathbf{H}}_{E,1}^{(n)}[t]$ and $\widehat{\mathbf{H}}_{E,2}^{(n)}[t]$ represent two estimated CSI values obtained by using Q_1 and Q_2 bits, respectively. Then, we can show that the following monotonicity result of the conjugate

[4] Due to this fact, the effective channel $\mathbf{H}_E^{(n)}[t] \in \mathbb{C}^{M_{\mathrm{RF}}^{\mathrm{M}} \times M_{\mathrm{RF}}^{\mathrm{B}}}$ under hybrid beamforming is usually low-rank ($M_{\mathrm{RF}}^{\mathrm{M}}$ and $M_{\mathrm{RF}}^{\mathrm{B}}$ are the numbers of RF chains at MS and BS, respectively). However, as long as $\mathbf{H}_E^{(n)}[t]$ is not rank one (i.e., having two or more non-zero singular values), then since $M_{\mathrm{RF}}^{\mathrm{M}} \ll M_{\mathrm{RF}}^{\mathrm{B}}$ under the large antenna array adopted in mmWave transmitter at the base station, then the rows in $\mathbf{H}_E^{(n)}[t]$ are close to orthogonal to each other from random matrix theory (see [29]).

beamforming achievable rate holds under limited CSI, which will be used in our subsequent analysis (the proof is relegated to [30] due to space limitation):

Lemma 2 (Monotonicity of beamforming achievable rate)**.** *If* $Q_1 \leq Q_2$*, then there exists a CSI quantization scheme under which* $\widehat{r}_n^{Q_1}[t] \leq \widehat{r}_n^{Q_2}[t]$*. Further,* $\widehat{r}_n^{Q}[t] \uparrow r_n[t]$ *as* $Q \to \infty$*.*

3) Algorithmic Changes to the QCS Framework: Due to the use of Q-bit limited CSI in mmWave hybrid beamforming, we modify the QCS algorithmic framework in Algorithm 1 accordingly as follows:

Algorithm 2: Queue-Length-Based Congestion Control and Scheduling in mmWave Cellular Network with Q-Bit CSI.

Initialization: Choose parameters $\epsilon > 0$. Set $t = 0$.
Main Loop:

1. *MaxWeight Scheduler:* In time-slot $t \geq 1$, given the queue-length vector $\mathbf{q}[t]$ and the Q-bit estimated CSI $\widehat{\mathbf{H}}_E^{(n)}[t]$, $\forall n$, we let $\tilde{r}_n[t]$ be the presumed conjugate beamforming achievable rate under $\widehat{\mathbf{H}}_E^{(n)}[t]$, $\forall n$. Then, the scheduler chooses a user n such that $n = \arg\max_{n' \in \{1,\ldots,N\}}\{q_{n'}[t]\,\tilde{r}_{n'}[t]\}$. Thus, the actual achievable service rates are $s_{Q,n}[t] = \widehat{r}_n^{Q}[t]$ and $s_{Q,n'}[t] = 0$, $\forall n' \neq n$.
2. *Congestion Controller:* Same as in Algorithm 1.
3. *Queue-Length Updates:* Same as in Algorithm 1.

---

4) Performance Analysis: For better readability, we structure our performance analysis into the following key steps:

Step 1) A Deterministic Joint Congestion Control and Scheduling Problem: To describe our main theoretical results, we first need the following deterministic problem, where we assume that the channel state process is not random and fixed at its mean. We let $\bar{\mathcal{C}}^Q \triangleq \{r_n^Q, \forall n : r_n^Q = \mathbb{E}\{\widehat{r}_n^Q[t]\}\}$ denote the mean achievable rate region. Also, the congestion control and scheduling variables are time-invariant and denoted as a_n and $s_{Q,n}$, $\forall n$, respectively. Then, the deterministic congestion control and scheduling problem can be written as:

$$\text{Maximize}\left\{\frac{1}{\epsilon}\sum_{n=1}^{N}U_n(a_n)\;\middle|\;\begin{array}{l} a_n - s_{Q,n} \leq 0, \forall n, \\ s_{Q,n} \in \bar{\mathcal{C}}^Q, \forall n, \\ a_n \in [0, a^{\max}],\ \forall n. \end{array}\right\}. \quad (12)$$

Based on the convex approximation argument in Theorem 1, it is clear that Problem (12) is approximately convex. Associating dual variables $q_{Q,n} \geq 0$, $\forall n$ with the constraints $a_n - s_{Q,n} \leq 0$, $\forall n$, we obtain the Lagrangian as follows:

$$\Theta_\epsilon(\mathbf{q}_Q) \triangleq \max_{\mathbf{a},\mathbf{s}_Q \in \bar{\mathcal{C}}^Q}\left\{\frac{1}{\epsilon}\sum_{n=1}^{N}U_n(a_n) + \sum_{n=1}^{N}q_{Q,n}(s_{Q,n} - a_n)\right\},$$

where the notation $\Theta_\epsilon(\cdot)$ signifies the Lagrangian's dependence on ϵ and the vector $\mathbf{q}_Q \triangleq [q_{Q,1},\ldots,q_{Q,N}]^\top \in \mathbb{R}_+^N$ contains all dual variables. Then, the Lagrangian dual problem of Problem (12) can be written as:

$$\text{Minimize}\ \left\{\Theta_\epsilon(\mathbf{q}_Q)\,\middle|\,\mathbf{q}_Q \in \mathbb{R}_+^N\right\}. \quad (13)$$

It can be seen that since Problem (13) is unconstrained, the Slater condition [26] trivially holds if the primal problem is feasible. Therefore, the optimal value of Problem (12) can be obtained by solving the dual problem in (13) since the primal problem is approximately convex. Let $(\mathbf{a}_Q^*, \mathbf{s}_Q^*)$ and $\mathbf{q}_{Q,(\epsilon)}^*$ be the optimal primal and dual solutions to Problem (12) and Problem (13), respectively. Then, it can be shown that $\mathbf{q}_{Q,(\epsilon)}^*$ satisfies the following properties:

Lemma 3 (Dual solution)**.** $\mathbf{q}_{Q,(\epsilon)}^* = \frac{1}{\epsilon}\mathbf{q}_{Q,(1)}^*$*, i.e.,* $\mathbf{q}_{Q,(\epsilon)}^*$ *grows linearly and the slope depends on* $\mathbf{q}_{Q,(1)}^*$*. Further, if* $Q_1 \leq Q_2$*, then the slopes satisfy* $\mathbf{q}_{Q_1,(1)}^* \geq \mathbf{q}_{Q_2,(1)}^*$*.*

Lemma 3 can be proved by using the Karush-Kuhn-Tucker (KKT) conditions [26] (the proof is relegated to [30] due to space limitation). Also, note that ϵ is only a scaling factor in the objective function in (12). Then, by contradiction, we can show the following result (see [30] for proof details):

Lemma 4 (Primal solution)**.** *The congestion control solution* $\mathbf{a}_Q^*$ *is independent of* ϵ *and equal to the service rate* $\mathbf{s}_Q^*$*.*

With the results of the deterministic problem, we are in a position to analyze the delay and congestion control performance of the original stochastic problem.

Step 2) Delay Performance of the Original Stochastic Problem: With Lemmas 3 and 4, we are now ready to present the main results in this section. Our first result says that the steady-state queue-length vector $\mathbf{q}^\infty$ lies in a bounded neighborhood of the dual solution $\mathbf{q}_{Q,(\epsilon)}^*$ of Problem (13). Further, the size of the neighborhood manifests a phase-transition phenomenon (see proof details in Appendix C).

Theorem 2 (Queueing delay phase transition)**.** *Under Algorithm 2 with any given Q-bit CSI quantization scheme, there exists a critical value* $Q^\sharp$ *independent of the performance control parameter* ϵ *of Algorithm 2, such that:*

- *If* $0 < Q < Q^\sharp$*, then* $\mathbb{E}\{\|\mathbf{q}^\infty - \mathbf{q}_{Q,(\epsilon)}^*\|\} = O(C_{(Q)}\frac{1}{\epsilon})$*, where* $C_{(Q)} \geq 0$ *is a constant depending on the quantization codebook, and* $C_{(Q)}$ *decreases as Q increases;*
- *If* $Q \geq Q^\sharp$*, then* $\mathbb{E}\{\|\mathbf{q}^\infty - \mathbf{q}_{Q,(\epsilon)}^*\|\} = O(1/\sqrt{\epsilon})$*.*

Remark 2. Theorem 2 and Lemma 3 characterize the steady-state queue-length scalings: If Q is larger than the critical value $Q^\sharp$, the steady state queue-length deviation grows sublinearly, which is much slower compared to the linear growth when $Q \leq Q^\sharp$. Also, the slope of mean queue-length $\mathbf{q}_{Q,(\epsilon)}^*$ depends on Q: the smaller the value of Q (i.e., poorer CSI accuracy), the steeper the slope. Note that the $O(1/\sqrt{\epsilon})$-scaling of queue-length deviation when $Q \geq Q^\sharp$ is the same as that under the full CSI case [15]. This shows a somewhat unexpected insight that full CSI is not necessary to produce (in order sense) the original QCS queue-length scaling behavior. ☐

Step 3) Congestion Control Performance of the Original Stochastic Problem: Now, let $a_{Q,n}^\infty \triangleq \mathbb{E}\{\min\{U_n^{'-1}(\epsilon q_n^\infty), a^{\max}\}\}$, $\forall n$, be the steady-state congestion control rates under a given Q-bit CSI quantization scheme and let $\mathbf{a}_Q^\infty \triangleq [a_{Q,1}^\infty, \ldots, a_{Q,N}^\infty]^\top$. The next main result characterizes the phase transition of the scaling of $\mathbf{a}_Q^\infty$'s deviation from the solution $\mathbf{a}_Q^*$ of Problem (12) (see Appendix D for proof details):

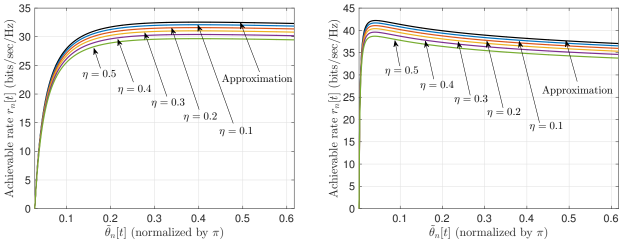

(a) $T_p/T = 0.01$. (b) $T_p/T = 0.001$.

Fig. 7. The approximation gaps of Problem (10) under different analog slide lobe gains η.

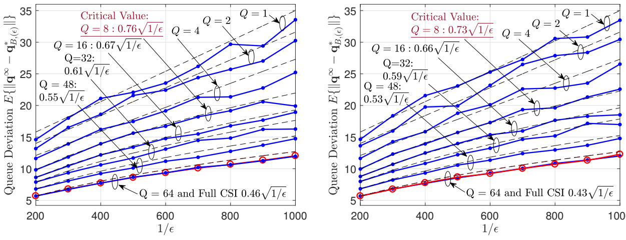

(a) SNR = 20 dB. (b) SNR = 30 dB.

Fig. 8. Average queue-length deviation with respect to $1/\epsilon$ for $Q = 1, 2, 4, 8, 16, 32, 48, 64$ bits ($M_{\mathrm{RF}}^{\mathrm{B}} = 80$).

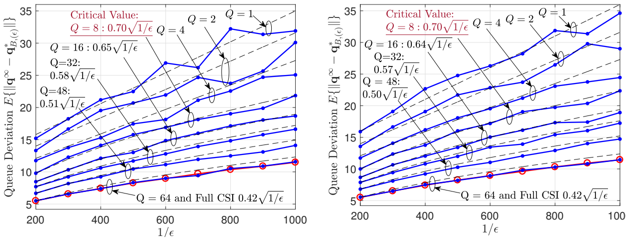

(a) SNR = 20 dB. (b) SNR = 30 dB.

Fig. 9. Average queue-length deviation with respect to $1/\epsilon$ for $Q = 1, 2, 4, 8, 16, 32, 48, 64$ bits ($M_{\mathrm{RF}}^{\mathrm{B}} = 90$).

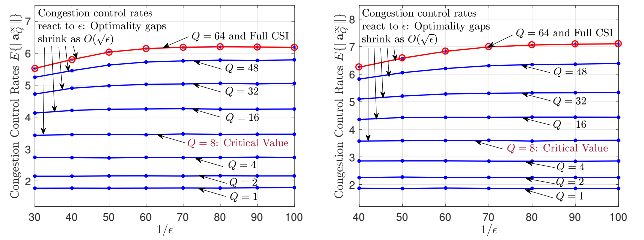

(a) SNR = 20 dB. (b) SNR = 30 dB.

Fig. 10. The congestion control rates with respect to $1/\epsilon$ for $Q = 1, 2, 4, 8, 16, 32, 48, 64$ bits. ($M_{\mathrm{RF}}^{\mathrm{B}} = 80$).

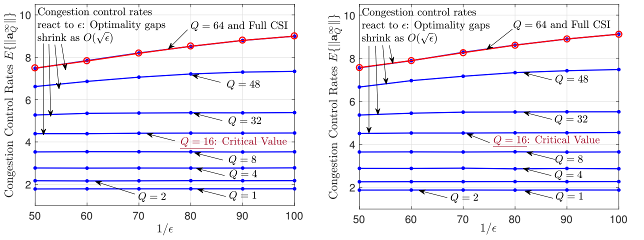

(a) SNR = 20 dB. (b) SNR = 30 dB.

Fig. 11. The congestion control rates with respect to $1/\epsilon$ for $Q = 1, 2, 4, 8, 16, 32, 48, 64$ bits. ($M_{\mathrm{RF}}^{\mathrm{B}} = 90$).

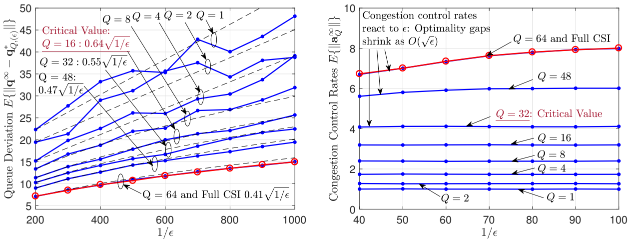

(a) SNR = 40 dB. (b) SNR = 20 dB.

Fig. 12. The queue-length deviation and congestion control rates with respect to $1/\epsilon$ for $Q = 1, 2, 4, 8, 16, 32, 48, 64$ bits. ($M_{\mathrm{RF}}^{\mathrm{B}} = 100$, 10 users).

Theorem 3 (Congestion control phase transition)**.** *Under Algorithm 2 with any Q-bit CSI quantization scheme, there exists a critical value $Q^\sharp$, same as in Theorem 2, such that:*

- *If $0 < Q < Q^\sharp$, then $\|\mathbf{a}_Q^\infty - \mathbf{a}_Q^*\| = O(C_{(Q)})$, where $C_{(Q)} \geq 0$ is the same constant as defined in Theorem 2;*
- *If $Q \geq Q^\sharp$, then $\|\mathbf{a}_Q^\infty - \mathbf{a}_Q^*\| = O(\sqrt{\epsilon})$.*

Remark 3. Theorem 3 also indicates a phase transition for $\mathbf{a}_Q^\infty$: When $Q < Q^\sharp$, the performance control parameter ϵ of Algorithm 2 has no effect on the deviation $\|\mathbf{a}_Q^\infty - \mathbf{a}_Q^*\|$. However, when $Q \geq Q^\sharp$, $\mathbf{a}_Q^\infty$'s deviation from $\mathbf{a}_Q^*$ grows as $O(\sqrt{\epsilon})$, which is the same as the full CSI case [14], [15]. Another way to interpret this phase transition phenomenon is that $Q^\sharp$ represents the minimum codebook size for a CSI quantization scheme, such that it can resurrect the performance tuning capability of parameter ϵ in the QCS algorithm. Both Theorems 2 and 3 can be proved by Lyapunov stability analysis, and the details are relegated to the appendix. □

VI. Numerical Results

In this section, we conduct simulations to demonstrate the theoretical results in Sections IV and V. We first verify the approximation accuracy and the pseudoconvexity of Problem (10). We set SNR to 30 dB and set the T_p/T ratios to 0.01 and 0.001. We vary the side lobe gain η from 0.1 to 0.5 and the results are shown in Figs. 7(a) and 7(b). We can see that, under both T_p/T ratios, the approximation gaps shrinks as η decreases. In these examples, the gaps under $\eta = 0.1$ are almost negligible. Moreover, we note that the approximation function is indeed pseudoconcave, as predicted by Theorem 1.

Next, we examine the impacts of CSI quality, characterized by the number of quantization bits Q, on the queue-lengths and the results are shown in Figs. 8 to 11. The number of users is set to five. In Figs. 8(a) and 8(b), we suppose that the BS and each MS have 80 and 2 RF chains, respectively, and we set the total SNR to be 20 dB and 30 dB, respectively. We use $\log(\cdot)$ as the utility function for each user (i.e., the proportional fairness metric [16]) and adopt random vector quantization (RVQ) as our Q-bit CSI quantization codebook [25]. We set the value of Q to be 1, 2, 4, 8, 16, 32, 48, and 64. We also draw an accompanying dash line to show the scaling trend of each curve in Fig. 8(a). For small Q values, we can see that the mean queue-length deviation increases faster than the square root law, roughly displaying a linear scaling with respect to ϵ as indicated in Theorem 2. For this example, the critical value of Q turns out to be 8. Once $Q \geq 8$, the queue-length deviations scale as $O(1/\sqrt{\epsilon})$, also confirming Theorem 2. In Figs. 9(a) and 9(b), we increase the number of RF chains at the BS to 90 and run the experiments under total SNR 20 dB and 30 dB again, respectively. Compared to Fig. 8, we can see that the same trends still hold under larger number of RF chains and the queue-length deviation is slightly smaller. This shows that the system delay performance is mostly limited by the number of RF chains at the MSs, hence the minor improvements. Also, when SNR is increased from 20 dB to 30 dB, we can see that the queue-deviation (i.e., delay) slightly decreases.

In Figs. 10(a) and 10(b), we study the impacts of Q-bit CSI on the congestion control rates. In Figs. 10(a) and 10(b), we suppose that the BS and each MS have 80 and 2 RF chains, respectively, and we set the total SNR to be 20 dB and 30 dB, respectively. For small Q values, we can see that $\mathbf{a}_Q^{\infty}$ is only affected by Q and is a constant independent of ϵ. Also, $\mathbf{a}_Q^{\infty}$'s gap to the full CSI case shrinks as Q increases, which confirms Lemma 4 and Theorem 3. Again, we can observe that the critical value of Q is 8: When $Q \geq 8$, $\mathbf{a}_Q^{\infty}$ displays an $O(\sqrt{\epsilon})$ diminishing gap to $\mathbf{a}_Q^{*}$, which agrees with Theorem 3. In Figs. 11(a) and 11(b), we increase the number of RF chains at the BS to 90 and run the experiments under total SNR 20 dB and 30 dB again, respectively. Again, compared to Fig. 10, we can see that the same trends still hold under larger number of RF chains and the queue-length deviation is slightly smaller. This shows that the system delay performance is mostly limited by the number of RF chains at the MSs, hence the minor improvements. Also, when SNR is increased from 20 dB to 30 dB, we can see that the congestion control rate increases, which is due to the increase of channel capacity.

Lastly, we change the number of users to ten and repeat the same set of experiments as in Figs. 8 to 11, and the results are illustrated in Figs. 12(a) and 12(b). We can see from Figs. 12(a) and 12(b) that the same trends of queue-length deviation and congestion control rates continue to hold under the setting with 10 users. In Fig. 12(a), the queue-length deviation is larger compared to the settings with five users when Q is small, which shows that delay performance is more sensitive to CSI quality as the number of users increases under mmWave hybrid beamforming. This is mainly due to the fact that under hybrid-beamforming, as the number of users increases, the duration of digital beamforming decreases as the number of users increases, hence smaller service rates compared to settings with fewer users. In Fig. 12(b), the congestion control rates (i.e., system throughput) is smaller compared to settings with five users when Q is small, which shows that the throughput performance is also more sensitive to CSI quality as the number of users increases under mmWave hybrid beamforming.

VII. CONCLUSION

In this paper, we studied the impacts of hybrid beamforming on the delay and network utility performance in mmWave cellular network optimization. We proposed a queue-length-based hybrid beamforming scheduling and congestion control framework for mmWave network utility maximization. We first showed that the hybrid beamforming scheduling subproblem in this framework enjoys a hidden pseudoconvexity structure, which leads to simplified analog beam training design. We then characterized two phase transition phenomena in throughput and delay with respect to CSI accuracy in digital beamforming. Collectively, these results deepen our understanding of mmWave networking performances. Hybrid beamforming in mmWave networking is an exciting and under-explored research area. Our future directions include, e.g., multi-cell mmWave networks with hybrid beamforming, the impacts of CSI inaccuracy on limited RF chains at the BS side, etc.

APPENDIX A
PROOF OF LEMMA 1

For simplicity, we let $r_n[t]$ denote the objective function of Problem (9). Substituting (1) and (2) into $r_n[t]$ and using the defined constants, we can rewrite the objective function of Problem (9) as:

$$r_n[t] = \left(b_0 - \frac{b_1}{\theta_B[t]\theta_{\mathrm{M}}[t]}\right)\sum_{k=1}^{K}\log_2\Bigg(1+ \underbrace{\frac{2\pi-(2\pi-\theta_B[t])\eta}{\theta_B[t]}\cdot\frac{2\pi-(2\pi-\theta_{\mathrm{M}}[t])\eta}{\theta_{\mathrm{M}}[t]}}_{(\Delta)}\, c_n^{(k)}\Bigg). \tag{14}$$

Note that the term (Δ) can be further written as:

$$(\Delta) = \left(\frac{2\pi(1-\eta)}{\theta_B[t]}+\eta\right)\left(\frac{2\pi(1-\eta)}{\theta_{\mathrm{M}}[t]}+\eta\right)$$
$$\overset{(a)}{=} \left(\frac{4\pi^2(1-\eta)^2}{\tilde{\theta}[t]} + \frac{2\pi(1-\eta)(\theta_B[t]+\theta_{\mathrm{M}}[t])}{\tilde{\theta}[t]} + \eta^2\right),$$

where in (a) we define $\tilde{\theta}[t] \triangleq \theta_B[t]\theta_{\mathrm{M}}[t]$. Now, we claim that

$$\frac{4\pi^2(1-\eta)^2}{\tilde{\theta}[t]} \gg \frac{2\pi(1-\eta)(\theta_B[t]+\theta_{\mathrm{M}}[t])}{\tilde{\theta}[t]}\eta \tag{15}$$

is true if $\eta \ll \frac{1}{3}$. To see this, we first note that $\eta \ll \frac{1}{3}$ implies $4\pi \ll \frac{2\pi(1-\eta)}{\eta}$. Also, since $\theta_B[t], \theta_{\mathrm{M}}[t] \in (0, 2\pi]$, we have

$$\theta_B[t]+\theta_{\mathrm{M}}[t] \leq 4\pi \ll \frac{2\pi(1-\eta)}{\eta},$$

which implies that (15) is true. Hence, it follows from (15) and $\eta \ll \frac{1}{3} < 1$ that $(\Delta) \approx (\frac{4\pi^2}{\tilde{\theta}[t]} + \eta^2)$, which further implies

$$r_n[t] = (14) \approx \left(b_0 - \frac{b_1}{\tilde{\theta}[t]}\right)\sum_{k=1}^{K}\log_2\left(1+\frac{4\pi^2 c_n^{(k)}}{\tilde{\theta}[t]}\right),$$

i.e., the objective function in (10). This completes the proof.

APPENDIX B
PROOF OF THEOREM 1

As mentioned earlier, verifying the pseudoconvexity of Problem (10) means verifying the pseudoconcavity of the objective function. Toward this end, we let $f(\tilde{\theta}[t])$ denote the *negative* objective function and our goal is to show that $f(\tilde{\theta}[t])$ is pseudoconvex, which means that for any $\tilde{\theta}_1[t]$ and $\tilde{\theta}_2[t]$ in the feasible interval, if$f'(\tilde{\theta}_1[t])(\tilde{\theta}_2[t]-\tilde{\theta}_1[t]) \geq 0$, we must also have $f'(\tilde{\theta}_2[t])(\tilde{\theta}_2[t]-\tilde{\theta}_1[t]) \geq 0$.

First, let us consider the case where $\tilde{\theta}_2[t] \geq \tilde{\theta}_1[t]$. Then, showing $f'(\tilde{\theta}_2[t])(\tilde{\theta}_2[t]-\tilde{\theta}_1[t]) \geq 0$ is equivalent to showing $f'(\tilde{\theta}_2[t]) \geq 0$. Note that, in this case, the condition $f'(\tilde{\theta}_1[t])(\tilde{\theta}_2[t]-\tilde{\theta}_1[t]) \geq 0$ simply means $f'(\tilde{\theta}_1[t]) \geq 0$, i.e.,

$$f'(\tilde{\theta}_1[t]) = \sum_{k=1}^{K} \frac{1}{\tilde{\theta}_1^2} \Bigg[\underbrace{\frac{4\pi^2 c_n^{(k)}}{\ln(2)} \cdot \frac{b_0\tilde{\theta}_1[t]-b_1}{\tilde{\theta}_1[t]+4\pi^2 c_n^{(k)}}}_{(P1)} - \underbrace{b_1 \log_2\left(1+\frac{4\pi^2 c_n^{(k)}}{\tilde{\theta}_1[t]}\right)}_{(P2)} \Bigg] \geq 0. \quad (16)$$

It is obvious that the term $(P2)$ is an increasing function of $\tilde{\theta}[t]$. Now, consider the fractional term $\frac{b_0\tilde{\theta}_1[t]-b_1}{\tilde{\theta}_1[t]+4\pi^2 c_n^{(k)}}$ in $(P1)$, which is negative-valued according to the definitions of b_0, b_1, and the feasible interval. Also, from the definition of b_0, we have $b_0 < 1$, implying that the absolute value of the nominator is increasing at a slower rate than that of the denominator. This means that $(P1)$ is also an increasing function of $\tilde{\theta}[t]$. Hence, $f'(\tilde{\theta}[t])$ is increasing since both $(P1)$ and $(P2)$ are increasing. As a result, $f'(\tilde{\theta}_1[t]) \geq 0$ and $\tilde{\theta}_2[t] \geq \tilde{\theta}_1[t]$ imply $f'(\tilde{\theta}_2[t]) \geq 0$ and thus the case of $\tilde{\theta}_2[t] \geq \tilde{\theta}_1[t]$ is proved. The other case where $\tilde{\theta}_2[t] \leq \tilde{\theta}_1[t]$ can also be proved by similar arguments and we omit the details in here for brevity.

To show that the optimal solution is unique and achieved in the interior of the feasible interval, it suffices to show that $\frac{\partial r_n[t]}{\partial \tilde{\theta}[t]}$'s values at two end points of the interval have opposite signs. Then, from the decreasing derivative property of $r_n[t]$ ($r_n[t] = -f(\tilde{\theta}[t])$), $\frac{\partial r_n[t]}{\partial \tilde{\theta}[t]}$ must have exactly one zero-crossing point in the interior of the feasible interval. Also, the pseudoconcavity of $r_n[t]$ means that the zero-crossing point is the global maximum. First, if $\tilde{\theta}[t] = \frac{b_1}{b_0}$, we have $(P1) = 0$. Hence, $\frac{\partial r_n[t]}{\partial \tilde{\theta}[t]} > 0$ since $-(P2) > 0$ (because b_1, $\tilde{\theta}^2[t]$, and the $\log(\cdot)$ rate expressions are positive). On the other hand, when $\tilde{\theta}[t] \uparrow \psi_n^{\mathrm{B}}\psi_n^{\mathrm{M}}$, it follows from $T_p \ll T$ that

$$\begin{aligned} r_n[t] =& \left[1 - \left(N\beta + \frac{\sum_{n'=1}^{N} \psi_{n'}^{\mathrm{B}}\psi_{n'}^{\mathrm{M}}}{\psi_n^{\mathrm{B}}\psi_n^{\mathrm{M}}}\right)\frac{T_p}{T}\right] \times \\ & \sum_{k=1}^{K} \log_2\left(1+\frac{4\pi^2 c_n^{(k)}}{\tilde{\theta}[t]}\right) \\ \approx & \sum_{k=1}^{K} \log_2\left(1+\frac{4\pi^2 c_n^{(k)}}{\tilde{\theta}[t]}\right), \end{aligned}$$

which is decreasing in $\tilde{\theta}[t]$ and must have a negative derivative at $\tilde{\theta}[t] = \psi_n^{\mathrm{B}}\psi_n^{\mathrm{M}}$. This completes the proof.

APPENDIX C
PROOF OF THEOREM 2

To prove Theorem 2, we first show the existence of steady-state by proving a positive Harris-recurrence result of the queue-length process. This result implies the existence of steady-state, which lays the foundation for proving Theorems 2. We let $\mathbb{1}_{\mathcal{A}}(\mathbf{x})$ denote the indicator function, which takes value 1 if $\mathbf{x} \in \mathcal{A}$ and 0 otherwise. We state the queue-length positive Harris-recurrence result as follows:

Proposition 1 (Queue-Length Positive Recurrence)**.** *Consider a Lyapunov function* $V(\mathbf{q}[t]) \triangleq \frac{\epsilon}{2}\|\mathbf{q}[t]-\mathbf{q}^*_{Q,(\epsilon)}\|^2$ *for a given* ϵ*. For the scheduler (5) and congestion controller (6)–(7), there exist constants* $\delta, \eta > 0$*, both independent of* ϵ*, such that the queue-length process* $\{\mathbf{q}[t]\}_{t=0}^{\infty}$ *satisfies the following conditional mean drift condition:*

$$\begin{aligned} &\mathbb{E}\{\Delta V(\mathbf{q}[t]|\mathbf{q}[t])\} \triangleq \mathbb{E}\{V(\mathbf{q}[t+1]) - V(\mathbf{q}[t])|\mathbf{q}[t]\} \\ &\quad \leq -\frac{\epsilon\delta}{\Phi}\|\mathbf{q}[t]-\mathbf{q}^*_{Q,(\epsilon)}\|\mathbb{1}_{\mathcal{Q}^c}(\mathbf{q}[t]) + \eta\mathbb{1}_{\mathcal{Q}}(\mathbf{q}[t]), \end{aligned} \quad (17)$$

where $\mathcal{Q} \triangleq \{\mathbf{q} \in \mathbb{Z}_+^N | \|\mathbf{q}-\mathbf{q}^*_{Q,(\epsilon)}\| \leq \gamma/\epsilon\}$ *for some constant* $\gamma > 0$ *and* $\mathcal{B}^c$ *denotes the complement of* $\mathcal{Q}$ *in* $\mathbb{Z}_+^N$*.*

Proof. Consider the quadratic Lyapunov function defined in Proposition 1: $V(\mathbf{q}[t]) = \frac{\epsilon}{2}\|\mathbf{q}[t]-\mathbf{q}^*_{Q,(\epsilon)}\|^2$, where $\mathbf{q}[t]$ represents the queue-length vector in time-slot t under parameters ϵ and Q; and $\mathbf{q}^*_{Q,(\epsilon)}$ denotes the optimal dual solution for the static version of Problem JCS under parameter ϵ. Then, the one-slot mean Lyapunov drift of $V(\mathbf{q}[t])$ can computed as:

$$\begin{aligned} &\mathbb{E}\{V(\mathbf{q}[t+1]) - V(\mathbf{q}[t])|\mathbf{q}[t]\} \\ &= \mathbb{E}\left\{\frac{\epsilon}{2}\|\mathbf{q}[t+1]-\mathbf{q}^*_{(\epsilon)}\|^2 - \frac{\epsilon}{2}\|\mathbf{q}[t]-\mathbf{q}^*_{Q,(\epsilon)}\|^2 \middle| \mathbf{q}[t]\right\} \\ &= \frac{\epsilon}{2}\mathbb{E}\left\{(\mathbf{q}[t+1]-\mathbf{q}[t])^\top(\mathbf{q}[t+1]+\mathbf{q}[t]-2\mathbf{q}^*_{Q,(\epsilon)}) \middle| \mathbf{q}[t]\right\} \\ &\overset{(a)}{\leq} \frac{\epsilon}{2}\mathbb{E}\left\{(-\mathbf{s}_Q[t]+\mathbf{a}[t])^\top(2\mathbf{q}[t]-2\mathbf{q}^*_{Q,(\epsilon)}-\mathbf{s}_Q[t]+\mathbf{a}[t]) \middle| \mathbf{q}[t]\right\} \\ &= \frac{\epsilon}{2}\mathbb{E}\left\{-\mathbf{s}_Q[t]+\mathbf{a}[t]\|^2+2(\mathbf{q}[t]-\mathbf{q}^*_{Q,(\epsilon)})^\top(-\mathbf{s}^Q[t]+\mathbf{a}[t]) \middle| \mathbf{q}[t]\right\} \\ &= \epsilon(\mathbf{q}[t]-\mathbf{q}^*_{Q,(\epsilon)})^\top(-\mathbf{s}_Q[t]+\mathbf{a}[t]) + \frac{\epsilon}{2}\mathbb{E}\left\{\|-\mathbf{s}_Q[t]+\mathbf{a}[t]\|^2\right\}, \end{aligned}$$

where (a) follows from the non-expansive property of the $\max\{0,\cdot\}$ operation. Note that, from the definition of Algorithm 1, we have $\mathbb{E}\{\|\mathbf{a}[t]\|^2|\mathbf{q}[t]\} < A_2^{\max}N$. Also, since $s_{Q,n}[t]$ falls in a bounded instantaneous capacity region $\mathcal{C}_{\widehat{\mathbf{H}}[t]}$, $\forall n$, we must have $s_{Q,n}[t] \leq s^{\max}$ for some $s^{\max} > 0$. Hence, by defining $D_0 \triangleq \frac{N}{2}(A_2^{\max}+(s^{\max})^2)$, we have

$$\begin{aligned} &\mathbb{E}\left\{\Delta V(\mathbf{q}[t])|\mathbf{q}[t]\right\} \leq \epsilon(\mathbf{q}[t]-\mathbf{q}^*_{Q,(\epsilon)})^\top\mathbb{E}\left\{\mathbf{a}[t]-\mathbf{s}_Q[t]\right\}+\epsilon D_0 \\ &\overset{(a)}{=} \epsilon(\mathbf{q}[t]-\mathbf{q}^*_{Q,(\epsilon)})^\top(\mathbb{E}\{\mathbf{a}[t]|\mathbf{q}[t]\}-\mathbf{s}^*_Q)+ \\ &\quad \epsilon\mathbb{E}\{(\mathbf{q}[t]-\mathbf{q}^*_{Q,(\epsilon)})^\top(\mathbf{s}^*_Q-\mathbf{s}_Q[t])|\mathbf{q}[t]\}+\epsilon D_0, \\ &\overset{(b)}{\leq} \epsilon(\mathbf{q}[t]-\mathbf{q}^*_{Q,(\epsilon)})^\top(\mathbb{E}\{\mathbf{a}[t]|\mathbf{q}[t]\}-\mathbf{s}^*_Q)+ \\ &\quad \epsilon\|\mathbf{q}[t]-\mathbf{q}^*_{Q,(\epsilon)}\|\mathbb{E}\{\|\mathbf{s}^*_Q-\mathbf{s}_Q[t]\||\mathbf{q}[t]\}+\epsilon D_0, \end{aligned} \quad (18)$$

where $\mathbf{s}^*_Q$ is such that $(\mathbf{s}^*_Q, \mathbf{q}^*_{Q,(\epsilon)})$ is a pair of optimal primal and dual solutions to Problem (13) under parameter ϵ. In (18), (a) follows from adding and subtracting $\mathbf{s}^*_Q$ as well as the fact that $\mathbf{a}[t]$ is independent of the channel state and determined solely by $\mathbf{q}[t]$; and (b) follows from Cauchy-Schwarz inequality.

Note from Lemma 4 that $\mathbf{s}_Q^*$ is independent of ϵ and $s_{Q,n}[t] \in \mathcal{C}_{\widehat{\mathbf{H}}[t]}$ is upper-bounded. Thus, we have

$$\mathbb{E}\big\{\|\mathbf{s}_Q^* - \mathbf{s}_Q[t]\| |\mathbf{q}[t]\big\} \le C_{(Q)} \triangleq \max_{\mathbf{q}:\|\mathbf{q}\|=1} \mathbb{E}\{\|\mathbf{s}_Q^* - \mathbf{s}_Q\| \mathbf{q}\}, \quad (19)$$

where $C_{(Q)}$ signifies that its value depends on Q. Hence, we can further upper bound (18) as:

$$\begin{aligned}\mathbb{E}\left\{\Delta V(\mathbf{q}[t])|\mathbf{q}[t]\right\} &\le \epsilon(\mathbf{q}[t] - \mathbf{q}_{Q,(\epsilon)}^*)^\top \times \\ &(\mathbb{E}\{\mathbf{a}[t]|\mathbf{q}[t]\} - \mathbf{s}_Q^*) + \epsilon\|\mathbf{q}[t] - \mathbf{q}_{Q,(\epsilon)}^*\| C_{(Q)} + \epsilon D_0, \quad (20)\end{aligned}$$

Now, let us consider the first term on the right hand side in (20), i.e., $\epsilon(\mathbf{q}[t] - \mathbf{q}_{Q,(\epsilon)}^*)^\top(\mathbb{E}\{\mathbf{a}[t]|\mathbf{q}[t]\} - \mathbf{s}^*)$. Since $U_n(\cdot)$ is concave and increasing, $\forall n$, we have

$$\left(q_n[t] - q_{Q,(\epsilon),n}^*\right)^\top \left[U_n^{'-1}\left(\epsilon q_n[t]\right) - U_n^{'-1}\left(\epsilon q_{Q,(\epsilon),n}^*\right)\right] \le 0.$$

Thus, by the Cauchy-Schwatz inequality, we have:

$$\begin{aligned}&(\mathbf{q}[t] - \mathbf{q}_{Q,(\epsilon)}^*)^\top(\mathbb{E}\{\mathbf{a}[t]|\mathbf{q}[t]\} - \mathbf{s}_Q^*) \\ &= \sum_{n=1}^N \left(q_n[t] - q_{Q,(\epsilon),n}^*\right)^\top \left[U_n^{'-1}\left(\epsilon q_n[t]\right) - U_n^{'-1}\left(\epsilon q_{Q,(\epsilon),n}^*\right)\right] \\ &\le -\sum_{n=1}^N \left|q_n[t] - q_{Q,(\epsilon),n}^*\right| \left|U_n^{'-1}(\epsilon q_n[t]) - U_n^{'-1}\left(\epsilon q_{Q,(\epsilon),n}^*\right)\right|. (21)\end{aligned}$$

By the strong convexity of $-U_n(\cdot)$ and the Lipschitz continuity of $U_n'(\cdot)$, we have

$$\left|U_n'\left(a_{n,1}\right) - U_n'\left(a_{n,2}\right)\right| \le \Phi\left|a_{n,1} - a_{n,2}\right|.$$

Therefore, by the inverse function lemma, we have

$$\frac{1}{\Phi}\left|\epsilon q_n[t] - \epsilon q_{Q,(\epsilon),n}^*\right| \le \left|U_n^{'-1}\left(\epsilon q_n[t]\right) - U_n^{'-1}\left(\epsilon q_{Q,(\epsilon),n}^*\right)\right|.$$

Hence, we can further upper-bound (21) as:

$$\begin{aligned}&(\mathbf{q}[t] - \mathbf{q}_{Q,(\epsilon)}^*)^\top(\mathbb{E}\{\mathbf{a}[t]|\mathbf{q}[t]\} - \mathbf{s}_Q^*) \\ &\le -\frac{\epsilon}{\Phi}\sum_{n=1}^N \left(q_n[t] - q_{Q,(\epsilon),n}^*\right)^2 = -\frac{1}{\Phi\epsilon}\left\|\mathbf{q}[t] - \mathbf{q}_{Q,(\epsilon)}^*\right\|^2. \quad (22)\end{aligned}$$

Substituting (22) into (20), we have

$$\begin{aligned}\mathbb{E}\left\{\Delta V(\mathbf{q}[t])|\mathbf{q}[t]\right\} \le &-\frac{\epsilon^2}{\Phi}\left\|\mathbf{q}[t] - \mathbf{q}_{Q,(\epsilon)}^*\right\|^2 \\ &+ \epsilon\|\mathbf{q}[t] - \mathbf{q}_{Q,(\epsilon)}^*\| C_{(Q)} + \epsilon D_0. \quad (23)\end{aligned}$$

Now, suppose that $\left\|\mathbf{q}[t] - \mathbf{q}_{Q,(\epsilon)}^*\right\| \ge \gamma_1/\epsilon$, where β_1 will be specified shortly. Note also that we can choose $\epsilon \ge 1$, we have

$$\frac{1}{\|\mathbf{q}[t] - \mathbf{q}_{Q,(\epsilon)}^*\|} \le \frac{\epsilon}{\gamma_1} \le \frac{1}{\gamma_1}.$$

It then follows that (23) can be further upper bounded as:

$$\begin{aligned}&\mathbb{E}\{\Delta V(\mathbf{q}[t])|\mathbf{q}[t]\} = -\frac{\epsilon}{\Phi}\left\|\mathbf{q}[t] - \mathbf{q}_{Q,(\epsilon)}^*\right\| \cdot \epsilon\left\|\mathbf{q}[t] - \mathbf{q}_{Q,(\epsilon)}^*\right\| \\ &+ \epsilon\|\mathbf{q}[t] - \mathbf{q}_{Q,(\epsilon)}^*\| D_1 + \left\|\mathbf{q}[t] - \mathbf{q}_{Q,(\epsilon)}^*\right\| \frac{\epsilon D_0}{\left\|\mathbf{q}[t] - \mathbf{q}_{Q,(\epsilon)}^*\right\|} \\ &\le -\frac{\epsilon}{\Phi}\left\|\mathbf{q}[t] - \mathbf{q}_{Q,(\epsilon)}^*\right\|\Big(\gamma_1 - C_{(Q)}\Phi - \frac{D_0\Phi}{\gamma_1}\Big). \quad (24)\end{aligned}$$

By choosing γ_1 such that $\gamma_1 - D_1\Phi - \frac{D_0\Phi}{\gamma_1} > 0$, we have

$$\mathbb{E}\{\Delta V(\mathbf{q}[t])|\mathbf{q}[t]\} \le -\frac{\epsilon\hat{\delta_1}}{\Phi}\left\|\mathbf{q}[t] - \mathbf{q}_{Q,(\epsilon)}^*\right\| \quad (25)$$

where $\hat{\delta_1} = \gamma_1 - C_{(Q)}\Phi - \frac{D_0\Phi}{\gamma_1}$. Solving $\beta_1 - C_{(Q)}\Phi - \frac{D_0\Phi}{\beta_1} = 0$ and plugging in the obtained γ_1 to define a ball $\mathcal{B}_1 \triangleq \{\mathbf{q} : \left\|\mathbf{q} - \mathbf{q}_{Q,(\epsilon)}^*\right\| \le \frac{1}{2\epsilon}[(C_{(Q)}\Phi) + \sqrt{(C_{(Q)}\Phi)^2 + 4D_0\Phi}]\}$, we have

$$\mathbb{E}\{\Delta V(\mathbf{q}[t])|\mathbf{q}[t]\} \le -\epsilon\delta_1\left\|\mathbf{q}[t] - \mathbf{q}_{Q,(\epsilon)}^*\right\|, \text{ if } \mathbf{q}[t] \in \mathcal{B}_1^c, \quad (26)$$

where $\delta_1 \triangleq \frac{\hat{\delta_1}}{\Phi}$. On the other hand, when $\mathbf{q}[t] \in \mathcal{B}_1$, it is clearly true that $\mathbb{E}\{\Delta V(\mathbf{q}[t])|\mathbf{q}[t]\} \le \eta_1$ for some $\eta_1 > 0$. Combining these facts yields the following:

$$\mathbb{E}\{\Delta V(\mathbf{q}[t])|\mathbf{q}[t] = \mathbf{q}\} \le -\epsilon\delta_1\|\mathbf{q} - \mathbf{q}_{Q,(\epsilon)}^*\| \mathbb{1}_{\mathcal{B}_1^c}(\mathbf{q}) + \eta_1\mathbb{1}_{\mathcal{B}_1}(\mathbf{q}).$$

This completes the proof of Proposition 1. $\square$

The inequality in (17) suggests that the conditional mean drift is negative when the deviation of the queue-length vector $\mathbf{q}[t]$ away from $\mathbf{q}_{Q,(\epsilon)}^*$ is sufficiently large. Since (17) is just the Foster-Lyapunov criterion [31, Proposition I.5.3], $\{\mathbf{q}[t]\}_{t=0}^\infty$ is positive recurrent, we have that a steady-state distribution of queue-lengths exists. Thus, we let $\mathbf{q}^\infty$ denote the queue-length vector in steady-state. With Proposition 1, we are now in a position to prove Theorem 2.

Next, to prove Theorem 2, we use an α-parameterized quadratic Lyapunov function: $V_\alpha(\mathbf{q}[t]) = \frac{\epsilon^\alpha}{2}\|\mathbf{q}[t] - \mathbf{q}_{Q,(\epsilon)}^*\|^2$, where the parameter $\alpha \in \{0, 1\}$ and its value will be specified later. Following similar steps in the proof of Proposition 1, we can bound the conditional mean Lyapunov drift as follows:

$$\begin{aligned}&\mathbb{E}\{V_\alpha(\mathbf{q}[t+1]) - V_\alpha(\mathbf{q}[t])|\mathbf{q}[t]\} \\ &\overset{(a)}{\le} \epsilon^\alpha(\mathbf{q}[t] - \mathbf{q}_{Q,(\epsilon)}^*)^\top(\mathbb{E}\{\mathbf{a}[t]|\mathbf{q}[t]\} - \mathbf{s}_Q^*) + \\ &\quad \epsilon^\alpha\mathbb{E}\{(\mathbf{q}[t] - \mathbf{q}_{Q,(\epsilon)}^*)^\top(\mathbf{s}_Q^* - \mathbf{s}_Q[t])|\mathbf{q}[t]\} + \epsilon^\alpha D_0, \\ &\overset{(b)}{\le} \epsilon^\alpha\Big[-\frac{\epsilon}{\Phi}\left\|\mathbf{q}[t] - \mathbf{q}_{Q,(\epsilon)}^*\right\|^2 + D_0\Big] + \\ &\quad \epsilon^\alpha\mathbb{E}\Big\{(\mathbf{q}[t] - \mathbf{q}_{Q,(\epsilon)}^*)^\top(\mathbf{s}_Q^* - \mathbf{s}_Q[t])\big|\mathbf{q}[t]\Big\} \\ &\overset{(c)}{\le} \epsilon^\alpha\Big[-\frac{\epsilon}{\Phi}\left\|\mathbf{q}[t] - \mathbf{q}_{Q,(\epsilon)}^*\right\|^2 + D_0\Big] + \\ &\quad \epsilon^\alpha\mathbb{E}\Big\{(\mathbf{q}[t])^\top(\mathbf{s}^* - \mathbf{s}_Q[t])\big|\mathbf{q}[t]\Big\}, \quad (27)\end{aligned}$$

where $D_0 \triangleq \frac{N}{2}(A_2^{\max} + (s^{\max})^2)$ and $\mathbf{s}^* \triangleq \lim_{Q\to\infty}\mathbf{s}_Q^*$. In (27), (a) follows from adding and subtracting $\mathbf{s}_Q^*$; (b) follows from (22); and (c) follows from $\mathbf{s}_Q^* \le \mathbf{s}^*$ (by Lemma 2) and the scheduler design, which implies $(\mathbf{q}_{Q,(K)}^*)^\top\mathbf{s}_Q[t] \le (\mathbf{q}_{Q,(K)}^*)^\top\mathbf{s}_Q^*$. Next, consider the T-step conditional mean Lyapunov drift. For any $\mathbf{q}[0] \ge \mathbf{0}$, we have that

$$\begin{aligned}&\mathbb{E}\{V_\alpha(\mathbf{q}[T])|\mathbf{q}[0]\} - V_\alpha(\mathbf{q}[0]) \\ &= \sum_{t=0}^{T-1}\mathbb{E}\{V(\mathbf{q}[t+1]) - V(\mathbf{q}[t])|\mathbf{q}[0]\} \\ &\overset{(a)}{=} \sum_{t=0}^{T-1}\sum_{\mathbf{q}\in\mathcal{Z}_+^N}\big[\Pr(\mathbf{q}[t] = \mathbf{q}|\mathbf{q}[0]) \\ &\quad \mathbb{E}\big\{V_\alpha(\mathbf{q}[t+1]) - V_\alpha(\mathbf{q}[t])|\mathbf{q}[t] = \mathbf{q}\big\}\big]\end{aligned}$$

$$\overset{(b)}{\leq} \sum_{t=0}^{T-1} \sum_{\mathbf{q}\in\mathcal{Z}_+^N} \Pr(\mathbf{q}[t]=\mathbf{q}|\mathbf{q}[0]) \Big\{ \epsilon^{\alpha} \Big[-\frac{\epsilon}{\Phi} \big\|\mathbf{q}[t]-\mathbf{q}^*_{Q,(\epsilon)}\big\|^2$$
$$+ D_0 \Big] \Big\} + \sum_{t=0}^{T-1} \sum_{\mathbf{q}\in\mathcal{Z}_+^N} \Pr(\mathbf{q}[t]=\mathbf{q}|\mathbf{q}[0]) \times$$
$$\Big\{ \epsilon^{\alpha} \mathbb{E}\Big\{ \mathbf{q}^\top (\mathbf{s}^* - \mathbf{s}_Q[t]) \Big\} \Big\}, \tag{28}$$

where (a) follows from the fact that $\mathbf{q}[t]$ is a discrete state Markov chain in $\mathbb{Z}_+^N$ and (b) follows from (27). Note that for any $\mathbf{q}[t] \in \mathbb{Z}_+^N$, $\lim_{T\to\infty} \frac{1}{T} \sum_{t=0}^{T-1} \Pr(\mathbf{q}[t]=\mathbf{q}|\mathbf{q}[0]) = \pi_{\mathbf{q}}^{\infty}$, where $\pi_{\mathbf{q}}^{\infty}$ denotes the stationary distribution of the Markov chain $\mathbf{q}[t]$. Moving $V(\mathbf{q}[0])$ to the right hand side, dividing both sides by T, and letting $T \to \infty$ yields:

$$0 \leq J + \sum_{\mathbf{q}\in\mathbb{Z}_+^N} \pi_{\mathbf{q}}^{\infty} (\mathbf{q})^\top (\mathbf{s}^* - \mathbf{s}_B^{\infty}) = J + \mathbb{E}\big\{ (\mathbf{q}^{\infty})^\top (\mathbf{s}^* - \mathbf{s}_B^{\infty} \big\}, \tag{29}$$

where $J \triangleq \lim_{T\to\infty} \frac{1}{T} \sum_{t=0}^{T-1} \sum_{\mathbf{q}\in\mathcal{Z}_+^N} \Pr(\mathbf{q}[t] = \mathbf{q}|\mathbf{q}[0]) \{\epsilon^{\alpha}[\frac{-\epsilon}{\Phi} \|\mathbf{q}[t] - \mathbf{q}^*_{(\epsilon)}\|^2 + D_0]\}$, and $\mathbf{s}_Q^{\infty} \triangleq \arg\max_{\mathbf{x}\in\mathcal{C}_{\mathbf{H}[\infty]|\widehat{\mathbf{H}}[\infty]}} (\mathbf{q}^{\infty})^\top \mathbf{x}$ represents the steady-state service rates with Q-bit CSI.

Next, consider the term $\mathbb{E}\big\{(\mathbf{q}^{\infty})^\top(\mathbf{s}^* - \mathbf{s}_Q^{\infty})\big\}$ in (29). For any given realization of $\mathbf{q}^{\infty}$ in the steady-state, from the design of the MaxWeight scheduler in (5), we have that

$$(\mathbf{q}^{\infty})^\top \mathbf{s}^* \leq \max_{\mathbf{x}\in\mathcal{C}_{\mathbf{H}[\infty]}} (\mathbf{q}^{\infty})^\top \mathbf{x} = (\mathbf{q}^{\infty})^\top \mathbf{s}^{\infty}. \tag{30}$$

where $\mathbf{s}^{\infty} \triangleq \lim_{Q\to\infty} \mathbf{s}_Q^{\infty}$ and $\mathbf{H}[\infty]$ represent the full CSI in the steady state. Hence, for any realization of $\mathbf{q}^{\infty}$ such that $\mathbf{q}^{\infty} \neq \rho\mathbf{s}^*$ for some $\rho \in \mathbb{R}$, if Q is sufficiently large, we must have $(\mathbf{q}^{\infty})^\top\mathbf{s}^* - (\mathbf{q}^{\infty})^\top\mathbf{s}_Q^{\infty} \leq 0$. Hence, there exists a critical value $Q^{\sharp}$ such that for all $Q > Q^{\sharp}$, the average value of $(\mathbf{q}^{\infty})^\top\mathbf{s}^* - (\mathbf{q}^{\infty})^\top\mathbf{s}_Q^{\infty}$ can be made non-positive, i.e., $\mathbb{E}\big\{(\mathbf{q}^{\infty})^\top(\mathbf{s}^* - \mathbf{s}_Q^{\infty})\big\} \leq 0$. Hence, we consider two cases based on the positivity of $\mathbb{E}\big\{(\mathbf{q}^{\infty})^\top(\mathbf{s}^* - \mathbf{s}_Q^{\infty})\big\}$ as follows:

Case I): $Q \geq Q^{\sharp}$ such that $\mathbb{E}\big\{(\mathbf{q}^{\infty})^\top(\mathbf{s}^* - \mathbf{s}_Q^{\infty})\big\} \leq 0$: In this case, it follows from (29) that

$$0 \leq \lim_{T\to\infty} \frac{1}{T} \sum\nolimits_{t=0}^{T-1} \sum\nolimits_{\mathbf{q}\in\mathcal{Z}_+^N} \Pr(\mathbf{q}[t]=\mathbf{q}|\mathbf{q}[0])$$
$$\Big\{ \epsilon^{\alpha} \Big[-\frac{\epsilon}{\Phi} \big\|\mathbf{q}[t]-\mathbf{q}^*_{Q,(\epsilon)}\big\|^2 + D_0 \Big] \Big\}. \tag{31}$$

We now consider the term in the second line in (31) by setting $\alpha = 0$. Similar to the proof of Proposition 1, suppose that $\big\|\mathbf{q}[t] - \mathbf{q}^*_{Q,(\epsilon)}\big\| \geq \gamma/\sqrt{\epsilon}$, where γ will be specified shortly. This implies that $\frac{1}{\|\mathbf{q}[t]-\mathbf{q}^*_{Q,(\epsilon)}\|} \leq \frac{1}{\gamma}$. Then, the second line in (31) can be upper bounded as:

$$-\frac{\epsilon}{\Phi} \big\|\mathbf{q}[t]-\mathbf{q}^*_{Q,(\epsilon)}\big\|^2 + D_0$$
$$= -\frac{\sqrt{\epsilon}}{\Phi} \big\|\mathbf{q}[t]-\mathbf{q}^*_{Q,(\epsilon)}\big\| \Bigg(\sqrt{\epsilon}\|\mathbf{q}[t]-\mathbf{q}^*_{Q,(\epsilon)}\| + \frac{D_0\Phi}{\sqrt{\epsilon}\|\mathbf{q}[t]-\mathbf{q}^*_{Q,(\epsilon)}\|} \Bigg)$$
$$\leq -\frac{\sqrt{\epsilon}}{\Phi} \big\|\mathbf{q}[t]-\mathbf{q}^*_{Q,(\epsilon)}\big\| \Big(\gamma - \frac{D_0\Phi}{\gamma} \Big). \tag{32}$$

Hence, by choosing $\gamma > \sqrt{D_0\Phi}$, we have

$$-\frac{\epsilon}{\Phi} \big\|\mathbf{q}[t]-\mathbf{q}^*_{Q,(\epsilon)}\big\|^2 + D_0 \leq -\frac{\sqrt{\epsilon}\hat{\delta}}{\Phi} \big\|\mathbf{q}[t]-\mathbf{q}^*_{Q,(\epsilon)}\big\|, \tag{33}$$

where $\hat{\delta} = \gamma - \frac{D_0\Phi}{\gamma} > 0$. Plugging in $\gamma > \sqrt{D_0\Phi}$ to define a ball $\mathcal{B} \triangleq \{\mathbf{q} : \|\mathbf{q} - \mathbf{q}^*_{Q,(\epsilon)}\| \leq \sqrt{D_0\Phi}/\sqrt{\epsilon}\}$, we have

$$-\frac{\epsilon}{\Phi} \big\|\mathbf{q}[t]-\mathbf{q}^*_{Q,(\epsilon)}\big\|^2 + D_0 \leq -\sqrt{\epsilon}\delta \|\mathbf{q}[t]-\mathbf{q}^*_{Q,(\epsilon)}\|, \text{ if } \mathbf{q}[t] \in \mathcal{B}^c.$$

On the other hand, when $\|\mathbf{q}[t] - \mathbf{q}^*_{Q,(\epsilon)}\| \leq \sqrt{D_0\Phi}/\sqrt{\epsilon}$, it is clear that $-(\epsilon/\Phi)\big\|\mathbf{q}[t] - \mathbf{q}^*_{Q,(\epsilon)}\big\|^2 + D_0 \leq \eta$ for some $\eta > 0$. Combining these facts, we have

$$-\frac{\epsilon}{\Phi} \big\|\mathbf{q}[t]-\mathbf{q}^*_{Q,(\epsilon)}\big\|^2 + D_0$$
$$\leq -\epsilon\delta \|\mathbf{q}[t] - \mathbf{q}^*_{Q,(\epsilon)}\| \mathbb{1}_{\mathcal{B}^c}(\mathbf{q}[t]) + \eta \mathbb{1}_{\mathcal{B}}(\mathbf{q}[t]). \tag{34}$$

Substituting (34) into (31) yields:

$$0 \leq \lim_{T\to\infty} \frac{1}{T} \sum_{t=0}^{T-1} \sum_{\mathbf{q}\in\mathcal{Z}_+^N} \Pr(\mathbf{q}[t]=\mathbf{q}|\mathbf{q}[0]) \times \tag{35}$$
$$\Big(-\epsilon\delta \|\mathbf{q}[t] - \mathbf{q}^*_{Q,(\epsilon)}\| \mathbb{1}_{\mathcal{B}^c}(\mathbf{q}) + \eta \mathbb{1}_{\mathcal{B}}(\mathbf{q}) \Big)$$
$$= \eta \sum_{\mathbf{q}\in\mathcal{B}} \pi_{\mathbf{q}}^{\infty} - \sqrt{\epsilon}\delta \sum_{\mathbf{q}\in\mathcal{B}^c} \|\mathbf{q} - \mathbf{q}^*_{Q,(\epsilon)}\| \pi_{\mathbf{q}}^{\infty}, \tag{36}$$

where we use the fact that, $\forall \mathbf{q} \in \mathcal{Z}_+^N$, $\lim_{T\to\infty} \frac{1}{T} \sum_{t=0}^{T-1} \Pr\{\mathbf{q}[t] = \mathbf{q}|\mathbf{q}[0]\} = \pi_{\mathbf{q}}^{\infty}$. Re-arranging the terms and with some manipulations, the above inequality can be written as:

$$\sqrt{\epsilon}\delta \sum_{\mathbf{q}\in\mathcal{Z}_+^N} \|\mathbf{q} - \mathbf{q}^*_{Q,(\epsilon)}\| \pi_{\mathbf{q}}^{\infty} \leq \sum_{\mathbf{q}\in\mathcal{B}} \Big(\eta + \sqrt{\epsilon}\delta \|\mathbf{q} - \mathbf{q}^*_{Q,(\epsilon)}\| \Big) \pi_{\mathbf{q}}^{\infty}$$
$$\leq (\eta + \delta\gamma) \sum_{\mathbf{q}\in\mathcal{B}} \pi_{\mathbf{q}}^{\infty} \leq (\eta + \delta\gamma), \tag{37}$$

where the second inequality follows from the definition of $\mathcal{B}$. Note here that the left-hand-side is precisely $\sqrt{\epsilon}\delta\mathbb{E}\{\|\mathbf{q}^{\infty} - \mathbf{q}^*_{Q,(\epsilon)}\|\}$. Thus, multiplying both sides by $1/\sqrt{\epsilon}\delta$, we have:

$$\mathbb{E}\{\|\mathbf{q}^{\infty} - \mathbf{q}^*_{Q,(\epsilon)}\|\} \leq \Big(\gamma + \frac{\eta}{\delta} \Big) \frac{1}{\sqrt{\epsilon}} = O\Big(\frac{1}{\sqrt{\epsilon}} \Big). \tag{38}$$

Case II): $Q \leq Q^{\sharp}$ such that $\mathbb{E}\big\{(\mathbf{q}^{\infty})^\top(\mathbf{s}^* - \mathbf{s}_Q^{\infty})\big\} > 0$: In this case, we set $\alpha = 1$. It thus follows from (27) that:

$$\mathbb{E}\big\{\Delta V_1(\mathbf{q}[t])|\mathbf{q}[t]\big\} \leq -\frac{\epsilon^2}{\Phi} \Big\|\mathbf{q}[t] - \mathbf{q}^*_{Q,(\epsilon)}\Big\|^2 +$$
$$\epsilon\|\mathbf{q}[t] - \mathbf{q}^*_{Q,(\epsilon)}\| C_{(Q)} + \epsilon D_0, \tag{39}$$

where $C_{(Q)}$ is defined in the proof of Proposition 1 (cf. Eq. (19)). Note that (39) is identical to (23). Then, following exactly the same steps as in the proof of Proposition 1, we have:

$$\mathbb{E}\{\Delta V_1(\mathbf{q}[t])|\mathbf{q}[t] = \mathbf{q}\} \leq -\epsilon\delta_1 \|\mathbf{q} - \mathbf{q}^*_{Q,(\epsilon)}\| \mathbb{1}_{\mathcal{B}_1^c}(\mathbf{q}) + \eta_1 \mathbb{1}_{\mathcal{B}_1}(\mathbf{q}).$$

where δ_1, η_1, and $\mathcal{B}_1$ are the same as in the proof of Proposition 1. Then, it follows from (28) that

$$\mathbb{E}\{V_1(\mathbf{q}[T]|\mathbf{q}[0])\} - V_1(\mathbf{q}[0]) \leq \eta_1 \sum_{\mathbf{q}\in\mathcal{B}_1} \sum_{t=0}^{T-1} \Pr\{\mathbf{q}[t] = \mathbf{q}|\mathbf{q}[0]\}$$
$$-\epsilon\delta_1 \sum_{\mathbf{q}\in\mathcal{B}_1^c} \|\mathbf{q} - \mathbf{q}^*_{(\epsilon)}\| \sum_{t=0}^{T-1} \Pr\{\mathbf{q}[t] = \mathbf{q}|\mathbf{q}[0]\}. \tag{40}$$

Following similar steps as in Case I to divide T on both sides on (40) and let $T \to \infty$, we have $0 \leq \eta_1 \sum_{\mathbf{q}\in\mathcal{B}_1} \pi_{\mathbf{q}}^{\infty} -$

$\epsilon\delta_1 \sum_{\mathbf{q}\in\mathcal{B}_1^c} \|\mathbf{q}-\mathbf{q}^*_{Q,(\epsilon)}\|\pi^\infty_{\mathbf{q}}$. Re-arranging the terms and with some manipulations, the above inequality can be written as:

$$\epsilon\delta_1 \sum_{\mathbf{q}\in\mathcal{Z}_+^N} \|\mathbf{q}-\mathbf{q}^*_{Q,(\epsilon)}\|\pi^\infty_{\mathbf{q}} \le \sum_{\mathbf{q}\in\mathcal{B}_1} \Big(\eta_1+\epsilon\delta_1\|\mathbf{q}-\mathbf{q}^*_{Q,(\epsilon)}\|\Big)\pi^\infty_{\mathbf{q}}$$

$$\le (\eta_1+\delta_1\gamma_1)\sum_{\mathbf{q}\in\mathcal{B}} \pi^\infty_{\mathbf{q}} \le (\eta_1+\delta_1\gamma_1),$$

where γ_1 is the same as in the proof of Proposition 1. Note that the left-hand-side is $\epsilon\delta_1\mathbb{E}\{\|\mathbf{q}^\infty-\mathbf{q}^*_{Q,(\epsilon)}\|\}$. Multiplying both sides by $\frac{1}{\epsilon\delta_1}$, we have:

$$\mathbb{E}\{\|\mathbf{q}^\infty-\mathbf{q}^*_{Q,(\epsilon)}\|\} \le \left(\gamma_1+\frac{\eta_1}{\delta_1}\right)\frac{1}{\epsilon}$$

$$= \left(\Big[(C_{(Q)}\Phi)+\sqrt{(C_{(Q)}\Phi)^2+4D_0\Phi}\Big]+\frac{\eta}{\delta}\right)\frac{1}{\epsilon} = O\bigg(C_{(Q)}\frac{1}{\epsilon}\bigg).$$

This completes the proof of Theorem 2.

APPENDIX D
PROOF OF THEOREM 3

To show the results in Theorem 3, we first note that $\mathbb{E}\{a_n[t]|q_n[t]\} = \min\{U_n^{'-1}(\epsilon q_n[t], A^{\max})\}$ and $a_n^* = U_n^{'-1}(\epsilon q_n^*)$, $\forall n$. Thus, we have:

$$\|\mathbf{a}^\infty_Q-\mathbf{a}^*_Q\| \le \|\mathbf{a}^\infty_Q-\mathbf{a}^*_Q\|_1$$

$$= \sum_{n=1}^N \bigg|\mathbb{E}\Big\{\min\Big\{U_n^{'-1}\Big(\epsilon q_n^\infty, A^{\max}\Big)\Big\}\Big\} - U_n^{'-1}\Big(\epsilon q^*_{Q,(\epsilon),n}\Big)\bigg|$$

$$\overset{(a)}{\le} \sum_{n=1}^N \mathbb{E}\bigg\{\Big|\min\Big\{U_n^{'-1}\Big(\epsilon q_n^\infty, A^{\max}\Big)\Big\} - U_n^{'-1}\Big(\epsilon q^*_{Q,(\epsilon),n}\Big)\Big|\bigg\}$$

$$\overset{(b)}{\le} \sum_{n=1}^N \mathbb{E}\bigg\{\Big|U_n^{'-1}\Big(\epsilon q_n^\infty\Big) - U_n^{'-1}\Big(\epsilon q^*_{Q,(\epsilon),n}\Big)\Big|\bigg\}$$

$$\overset{(c)}{=} \sum_{n=1}^N \mathbb{E}\bigg\{\Big|\Big[U_n^{'-1}\Big(\epsilon\tilde{q}_n\Big)\Big]'\Big(\epsilon q_n^\infty - \epsilon q^*_{Q,(\epsilon),n}\Big)\Big|\bigg\}$$

$$\overset{(d)}{\le} \sum_{n=1}^N \mathbb{E}\bigg\{\Big|\frac{1}{U_n''(\epsilon\tilde{q}_n)}\Big|\Big|\epsilon q_n^\infty - \epsilon q^*_{Q,(\epsilon),n}\Big|\bigg\}$$

$$\le \sum_{n=1}^N \mathbb{E}\bigg\{\frac{\epsilon}{\phi}|q_n^\infty - q^*_{Q,(\epsilon),n}|\bigg\} = \frac{\epsilon}{\phi}\mathbb{E}\big\{\|\mathbf{q}^\infty-\mathbf{q}^*_{Q,(\epsilon)}\|_1\big\}$$

$$\le \frac{\epsilon\sqrt{N}}{\phi}\mathbb{E}\big\{\|\mathbf{q}^\infty-\mathbf{q}^*_{Q,(\epsilon)}\|\big\}, \tag{41}$$

where (a) follows from Jensen's inequality and the convexity of the L^1-norm; (b) follows from relaxing the projection onto $[0, A^{\max}]$; (c) follows from the mean value theorem; and (d) follows from the inverse function lemma. Recall in the proof of Theorem 2 (cf. (29)), we have $0 \le J+\sum_{\mathbf{q}\in\mathbb{Z}_+^N}\pi^\infty_{\mathbf{q}}(\mathbf{q})^\top(\mathbf{s}^*-\mathbf{s}^\infty_Q) = J+\mathbb{E}\big\{(\mathbf{q}^\infty)^\top(\mathbf{s}^*-\mathbf{s}^\infty_Q)\big\}$. Again, based on the positivity of the term $\mathbb{E}\big\{(\mathbf{q}^\infty)^\top(\mathbf{s}^*-\mathbf{s}^\infty_Q)\big\}$, we consider two cases:

Case I): $Q > Q^\sharp$ such that $\mathbb{E}\big\{(\mathbf{q}^\infty)^\top(\mathbf{s}^*-\mathbf{s}^\infty_Q)\big\} \le 0$: In this case, we can again discard $\mathbb{E}\big\{(\mathbf{q}^\infty)^\top(\mathbf{s}^*-\mathbf{s}^\infty_Q)\big\}$ in (29) and let $\alpha = 0$ to obtain:

$$0 \le \lim_{T\to\infty}\frac{1}{T}\sum_{t=0}^{T-1}\sum_{\mathbf{q}\in\mathcal{Z}_+^N}\Pr(\mathbf{q}[t]=\mathbf{q}|\mathbf{q}[0])\times \Big\{-\frac{\epsilon}{\Phi}\big\|\mathbf{q}[t]-\mathbf{q}^*_{Q,(\epsilon)}\big\|^2\Big\}+D_0.$$

By re-arranging, multiplying both sides by Φ/ϵ, and noting that $\lim_{T\to\infty}\frac{1}{T}\sum_{t=0}^{T-1}\Pr\{\mathbf{q}[t]=\mathbf{q}|\mathbf{q}[0]\} = \pi^\infty_{\mathbf{q}}$, we have

$$\mathbb{E}\big\{\|\mathbf{q}^\infty-\mathbf{q}^*_{Q,(K)}\|^2\big\} \le D_0\Phi/\epsilon. \tag{42}$$

It then follows from (41) that

$$\|\mathbf{a}^\infty_Q-\mathbf{a}^*_Q\|^2 \le \left(\frac{\epsilon\sqrt{N}}{\phi}\mathbb{E}\big\{\|\mathbf{q}^\infty-\mathbf{q}^*_{Q,(\epsilon)}\|\big\}\right)^2 \overset{(a)}{\le}$$

$$\frac{\epsilon^2 N}{\phi^2}\mathbb{E}\big\{\|\mathbf{q}^\infty-\mathbf{q}^*_{Q,(\epsilon)}\|^2\big\} \overset{(b)}{\le} \frac{\epsilon^2 N}{\phi^2}D_0\frac{\Phi}{\epsilon} = \frac{\epsilon N D_0\Phi}{\phi^2}, \tag{43}$$

where (a) follows from Jensen's inequality; and (b) follows from (42). Taking square root on both sides of (43) yields $\|\mathbf{a}^\infty_Q-\mathbf{a}^*_Q\| = O(\sqrt{\epsilon})$.

Case II): $Q \le Q^\sharp$ such that $\mathbb{E}\big\{(\mathbf{q}^\infty)^\top(\mathbf{s}^*-\mathbf{s}^\infty_Q)\big\} > 0$: In this case, we set $\alpha = 1$ and it follows from (27) that:

$$\mathbb{E}\big\{\Delta V_1(\mathbf{q}[t])|\mathbf{q}[t]\big\} \le -\frac{\epsilon^2}{\Phi}\Big\|\mathbf{q}[t]-\mathbf{q}^*_{Q,(\epsilon)}\Big\|^2 +$$

$$\epsilon C_{(Q)}\|\mathbf{q}[t]-\mathbf{q}^*_{Q,(\epsilon)}\|+\epsilon D_0$$

$$= -\frac{\epsilon^2}{\Phi}\left(\|\mathbf{q}[t]-\mathbf{q}^*_{Q,(\epsilon)}\|-\frac{C_{(Q)}\Phi}{2\epsilon}\right)^2 + D, \tag{44}$$

where $C_{(Q)}$ is defined in the proof of Proposition 1 (cf. Eq. (19)) and $D \triangleq \frac{C_{(Q)}}{4}+\frac{\epsilon D_0}{\Phi}$. Telescoping the inequality in (44) from $t=0$ to $T-1$ yields:

$$\mathbb{E}\{V_1(\mathbf{q}[T]|\mathbf{q}[0])\}-V_1(\mathbf{q}[0]) \le -\frac{\epsilon^2}{\Phi}\sum_{t=0}^{T-1}\sum_{\mathbf{q}\in\mathbb{Z}_+^N}\Pr\{\mathbf{q}[t]=\mathbf{q}|\mathbf{q}[0]\}$$

$$\times\left(\|\mathbf{q}[t]-\mathbf{q}^*_{Q,(\epsilon)}\|-\frac{C_{(Q)}\Phi}{2\epsilon}\right)^2 + DT. \tag{45}$$

Dividing both sides of (45) by $\epsilon^2 T$, letting $T\to\infty$, and noting that $\lim_{T\to\infty}\frac{1}{T}\sum_{t=0}^{T-1}\Pr\{\mathbf{q}[t]=\mathbf{q}|\mathbf{q}[0]\} = \pi^\infty_{\mathbf{q}}$, $\forall\mathbf{q}\in\mathcal{Z}_+^N$, we have that:

$$\mathbb{E}\bigg\{\left(\|\mathbf{q}^\infty-\mathbf{q}^*_{Q,(\epsilon)}\|-\frac{C_{(Q)}\Phi}{2\epsilon}\right)^2\bigg\} \le \frac{D\Phi}{\epsilon^2}.$$

Taking square root on both sides yields:

$$\left[\mathbb{E}\bigg\{\left(\|\mathbf{q}^\infty-\mathbf{q}^*_{Q,(\epsilon)}\|-\frac{C_{(Q)}\Phi}{2\epsilon}\right)^2\bigg\}\right]^{\frac{1}{2}} \le \frac{\sqrt{D\Phi}}{\epsilon}. \tag{46}$$

Moreover, examining the left-hand-side of (46), we have

$$\left[\mathbb{E}\bigg\{\left(\|\mathbf{q}^\infty-\mathbf{q}^*_{Q,(\epsilon)}\|-\frac{C_{(Q)}\Phi}{2\epsilon}\right)^2\bigg\}\right]^{\frac{1}{2}}$$

$$\overset{(a)}{\ge} \mathbb{E}\bigg\{\left[\left(\|\mathbf{q}^\infty-\mathbf{q}^*_{Q,(\epsilon)}\|-\frac{C_{(Q)}\Phi}{2\epsilon}\right)^2\right]^{\frac{1}{2}}\bigg\}$$

$$= \mathbb{E}\bigg\{\Big|\|\mathbf{q}^\infty-\mathbf{q}^*_{Q,(\epsilon)}\|-\frac{C_{(Q)}\Phi}{2\epsilon}\Big|\bigg\}$$

$$\ge \mathbb{E}\bigg\{\|\mathbf{q}^\infty-\mathbf{q}^*_{Q,(\epsilon)}\|-\frac{C_{(Q)}\Phi}{2\epsilon}\bigg\}$$

$$= \mathbb{E}\big\{\|\mathbf{q}^\infty-\mathbf{q}^*_{Q,(\epsilon)}\|\big\}-\frac{C_{(Q)}\Phi}{2\epsilon}, \tag{47}$$

where (a) follows from Jensen's inequality. Combining (41), (46), and (47) yields:

$$\|\mathbf{a}^\infty_Q-\mathbf{a}^*_Q\| \le \frac{\epsilon\sqrt{N}}{\phi}\mathbb{E}\big\{\|\mathbf{q}^\infty-\mathbf{q}^*_{Q,(\epsilon)}\|\big\}$$

$$= \frac{\epsilon\sqrt{N}}{\phi}\left(\frac{C_{(Q)}\Phi}{2\epsilon}+\frac{\sqrt{D\Phi}}{\epsilon}\right) = O(C_{(Q)}).$$

Note that Cases I and II are exactly the same results as stated in Theorem 3. This completes the proof.

REFERENCES

[1] Y. Zhu, Z. Zhang, Z. Marzi, C. Nelson, U. Madhow, B. Y. Zhao, and H. Zheng, "Demystifying 60 GHz outdoor picocells," in *Proc. ACM MobiCom*, Maui, HI, September 2014, pp. 5 – 16.

[2] S. Sur, V. Venkateswaran, X. Zhang, and P. Ramanathan, "60 GHz indoor networking through flexible beams: A link-level profiling," in *Proc. ACM SIGMETRICS*, Portland, OR, June 2015, pp. 71–84.

[3] S. Rangan, T. S. Rappaport, and E. Erkip, "Millimeter-wave cellular wireless networks: Potentials and challenges," *Proceedings of the IEEE*, vol. 102, no. 3, pp. 366–385, mar 2014.

[4] H. Zhao, R. Mayzus, S. Sun, M. Samimi, J. K. Schulz, Y. Azar, K. Wang, G. N. Wong, F. Gutierrez, and T. S. Rappaport, "28 GHz millimeter wave cellular communication measurements for reflection and penetration loss in and around buildings in New York City," *IEEE Commun. Mag.*, vol. 51, no. 7, pp. 154–160, July 2013.

[5] Z. Pi and F. Khan, "An introduction to millimeter-wave mobile broadband systems," *IEEE Commun. Mag.*, vol. 49, no. 6, pp. 101–107, June 2011.

[6] A. Alkhateeb, O. E. Ayach, GeertLeus, and R. W. Heath, "Channel estimation and hybrid precoding for millimeter wave cellular systems," *IEEE J. Sel. Topics Signal Process.*, vol. 8, no. 5, pp. 831–846, October 2014.

[7] J. Wang et al., "Beam codebook based beamforming protocol formulti-Gbps millimeter-waveWPAN systems," *IEEE J. Sel. Areas Commun.*, vol. 27, no. 8, pp. 1390–1399, August 2009.

[8] S. Hur, T.Kim, D.Love, J. Krogmeier, T. Thomas, and A. Ghosh, "Millimeter wave beamforming for wireless backhaul and access in small cell networks," *IEEE Trans. Commun.*, vol. 61, no. 10, pp. 4391–4403, October 2013.

[9] S. Han, I. Chih-Lin, Z. Xu, and C. Rowell, "Large-scale antenna systems with hybrid analog and digital beamforming for millimeter wave 5G," *IEEE Commun. Mag.*, vol. 53, no. 1, pp. 186–194, Jan. 2015.

[10] X. Zhang, A. Molisch, and S. Kung, "Variable-phase-shift-based RF-baseband codesign for MIMO antenna selection," *IEEE Trans. Signal Process.*, vol. 53, no. 11, pp. 4091–4103, Nov. 2005.

[11] V. Venkateswaran and A. van der Veen, "Analog beamforming in MIMO communications with phase shift networks and online channel estimation," *IEEE Trans. Signal Process*, vol. 58, no. 8, pp. 4131–4143, Aug. 2010.

[12] O. E. Ayach, S. Rajagopal, S. Abu-Surra, Z. Pi, and R. W. Heath, "Spatially sparse precoding in millimeter wave MIMO systems," *IEEE Trans. Wireless Commun*, vol. 13, no. 3, pp. 1499–1513, Mar. 2013.

[13] T. Bogale, L. B. Le, A. Haghighat, and L. Vandendorpe, "On the number of RF chains and phase shifters, and scheduling design with hybrid analog-digital beamforming," *IEEE Trans. Wireless Commun.*, vol. 15, no. 5, pp. 3311–3326, May 2015.

[14] M. J. Neely, E. Modiano, and C.-P. Li, "Fairness and optimal stochastic control for heterogeneous networks," *IEEE/ACM Trans. Netw.*, vol. 16, no. 2, pp. 396–409, Apr. 2008.

[15] A. Eryilmaz and R. Srikant, "Fair resource allocation in wireless networks using queue-length-based scheduling and congestion control," *IEEE/ACM Trans. Netw.*, vol. 15, no. 6, pp. 1333–1344, Dec. 2007.

[16] X. Lin, N. B. Shroff, and R. Srikant, "A tutorial on cross-layer optimization in wireless networks," *IEEE J. Sel. Areas Commun.*, vol. 24, no. 8, pp. 1452–1463, Aug. 2006.

[17] J. Volakis, *Antenna Engineering Handbook, Fourth Edition*. McGraw-Hill Companies,Incorporated, 2007.

[18] H. Hashemi, X. Guan, A. Komijani, and A. Hajimiri, "A 24-GHz SiGe phased-array receiver-LO phase-shifting approach," *IEEE Transactions on Microwave Theory and Techniques*, vol. 53, no. 2, pp. 614–626, 2005.

[19] H. Steyskal, "Digital beamforming antennas: An introduction," *Microwave Journal*, vol. 30, no. 1, pp. 107–124, Jan. 1987.

[20] H. Steyskal and J. F. Rosel, "Digital beamforming for radar systems," *Microwave Journal*, vol. 32, no. 1, pp. 121–136, Jan. 1989.

[21] A. M. Hunter, J. G. Andrews, and S. Weber, "Transmission capacity of ad hoc networks with spatial diversity," *IEEE Trans. Wireless Commun.*, vol. 7, no. 12, pp. 5058–5071, Dec. 2008.

[22] J. Wildman, P. H. Nardelli, M. Latva-aho, and S. Weber, "On the joint impact of beamwidth and orientation error on throughput in wireless directional poisson networks," *IEEE Trans. Wireless Commun.*, vol. 13, no. 12, pp. 7072–7085, Jun. 2014.

[23] H. Shokri-Ghadikolaei, L. Gkatzikis, and C. Fischione, "Beam-searching and transmission scheduling in millimeter wave communications," in *Proc. IEEE ICC*, London, UK, Jun. 2015, pp. 1292 – 1297.

[24] E. G. Larsson, O. Edfors, and T. L. Marzetta, "Massive MIMO for next generation wireless systems," *IEEE Commun. Mag.*, vol. 52, no. 2, pp. 186–195, Feb. 2014.

[25] N. Jindal, "MIMO broadcast channels with finite rate feedback," *IEEE Trans. Inf. Theory*, vol. 52, no. 11, pp. 5045–5059, Nov. 2006.

[26] M. S. Bazaraa, H. D. Sherali, and C. M. Shetty, *Nonlinear Programming: Theory and Algorithms*, 3rd ed. New York, NY: John Wiley & Sons Inc., 2006.

[27] F. Rusek, D. Persson, B. K. Lau, E. G. Larsson, T. L. Marzetta, O. Edfors, and F. Tufvesson, "Scaling up MIMO: Opportunities and challenges with very large arrays," *IEEE Signal Process. Mag.*, vol. 30, no. 1, pp. 40–46, Jan. 2013.

[28] J. Liu, A. Eryilmaz, N. B. Shroff, and E. S. Bentley, "Understanding the impacts of limited channel state information on massive MIMO cellular network optimization," *IEEE Journal of Selected Areas in Communications (JSAC)*, vol. 35, no. 8, pp. 1715–1727, August 2017.

[29] M. Matthaiou, M. R. MacKay, P. J. Smith, and J. A. Nossek, "On the condition number distribution of complex Wishart matrices," *IEEE Trans. Commun.*, vol. 58, no. 6, pp. 1705–1717, Jun. 2010.

[30] J. Liu and E. S. Bentley, "Understanding the impacts of hybrid beamforming on millimeter wave cellular network performances," The Ohio State University, Tech. Rep., July 2016. [Online]. Available: https://www2.ece.ohio-state.edu/~liu/mmWave_HybridBF_SCH_TR.pdf?dl=0

[31] S. P. Meyn and R. L. Tweedie, *Markov Chains and Stochastic Stability*, 2nd ed. Cambridge, UK: Cambridge University Press, 2009.

Jia Liu (S'03–M'10–SM'16) received his Ph.D. degree in the Bradley Department of Electrical and Computer Engineering at Virginia Tech, Blacksburg, VA in 2010. He then joined the Department of Electrical and Computer Engineering at The Ohio State University as a Postdoctoral Researcher and subsequently a Research Assistant Professor. He is currently an Assistant Professor in the Department of Computer Science at Iowa State University, where he joined in Aug. 2017. His research areas include theoretical foundations of control and optimization for stochastic networked systems, distributed algorithms design, optimization of cyber-physical systems, data analytics infrastructure, and machine learning. Dr. Liu is a senior member of IEEE, a member of ACM, and a member of SIAM. His work has received numerous awards at top venues, including IEEE INFOCOM'19 Best Paper Award, IEEE INFOCOM'16 Best Paper Award, IEEE INFOCOM'13 Best Paper Runner-up Award, IEEE INFOCOM'11 Best Paper Runner-up Award, and IEEE ICC'08 Best Paper Award. He is a recipient of Bell Labs President Gold Award in 2001. He has served as a TPC member for IEEE INFOCOM since 2010 and a TPC member of ACM MobiHoc since 2017. His research has been supported by NSF, AFOSR, AFRL, and ONR.

Elizabeth S. Bentley has a B.S. degree in Electrical Engineering from Cornell University, a M.S. degree in Electrical Engineering from Lehigh University, and a Ph.D. degree in Electrical Engineering from University at Buffalo. She was a National Research Council Post-Doctoral Research Associate at the Air Force Research Laboratory in Rome, NY. Currently, she is employed by the Air Force Research Laboratory in Rome, NY, performing in-house research and development in the Networking Technology branch. Her research interests are in cross-layer optimization, wireless multiple-access communications, wireless video transmission, modeling and simulation, and directional antennas/directional networking.